ISSN 0801-9940 No. 01
March 2014

# A FINITE ELEMENT SOLVER FOR MODAL ANALYSIS OF MULTI-SPAN OFFSHORE PIPELINES

**by**

**Håvar Sollund and Knut Vedeld**

RESEARCH REPORT
IN MECHANICS


UNIVERSITY OF OSLO
DEPARTMENT OF MATHEMATICS
MECHANICS DIVISION

UNIVERSITETET I OSLO
MATEMATISK INSTITUTT
AVDELING FOR MEKANIKK

DEPT. OF MATH., UNIVERSITY OF OSLO
RESEARCH REPORT IN MECHANICS, No. 01
ISSN 0801-9940 March 2014

# A FINITE ELEMENT SOLVER FOR MODAL ANALYSIS OF MULTI-SPAN OFFSHORE PIPELINES

**by**

**Håvar Sollund and Knut Vedeld**

Mechanics Division, Department of Mathematics
University of Oslo, Norway

**Abstract.** Accurate determination of pipeline eigenfrequencies and mode shapes is essential to free span design. For pipelines resting on rough seabeds, multiple free spans are commonly located sufficiently close to be interacting, and finite element analysis (FEA) is then conventionally required to determine the modal response. In the present report, a tailor-made (specific purpose) FEA tool is developed to carry out modal analyses of multi-span offshore pipelines. The specific purpose FEA tool is thoroughly validated by comparisons to analytical results and to results obtained using the general purpose FEA software Abaqus. Several beam and pipeline configurations are studied, ranging from simplified analyses of simply supported beams to sophisticated analyses of challenging multi-span pipeline sections, using actual seabed survey data. The validation study therefore gives valuable insight into the dynamic response of multi-span subsea pipelines. Compared to general purpose FEA modeling, the specifically designed FEA tool offers more flexible adjustment of element resolution in critical areas, more efficient file storage utilization, and also allows the designer to improve aspects of the physical modeling. The latter includes the possibility of using a consistent soil stiffness formulation rather than a traditional lumped soil model with discrete springs, as well as applying different added mass coefficients in axial and transverse directions. The impact on the modal response quantities of adopting a consistent soil stiffness model and directional variation in added mass is investigated. In addition, a methodology for establishing the static configuration and the effective axial force distribution along the pipeline using the general purpose FEA software Abaqus is described.

**Keywords:** Modal analysis, Finite element analysis, Pipeline, Beam, Free span, Multi-spans

## TABLE OF CONTENTS

# 1 INTRODUCTION

Gaps between a pipeline and the seabed may occur due to scouring, uneven seabed and pipeline crossings. A pipeline is considered to be in a free span when there is, in-between two touchdown regions, a continuous gap between the seabed and the pipe. When a pipeline is in a free span, fluid flow induced by currents or waves or both, will cause vortices to be formed and shed in the wake of the flow [Sumer and Fredsøe, 2006]. The vortex shedding creates pressure oscillations in the horizontal and vertical directions perpendicular to the pipe axis. If the pressure oscillations occur at similar frequencies to the pipeline eigenfrequencies (in the horizontal or vertical directions) the pipeline will start to vibrate. This phenomenon is called vortex-induced vibrations (VIV) [Zdravkovich, 1997]. Such vibrations may threaten the integrity of pipelines and has, historically, been the cause of pipeline failures [Fyrileiv et al., 2005]. The vibration component in the direction of the flow is conventionally termed in-line VIV, while vibrations perpendicular to the flow are termed cross-flow VIV.

Since VIV occurs when pressure differentials due to vortex formation and shedding are similar to the eigenfrequencies of a pipe, the eigenfrequencies of a free span are fundamental design parameters in free span design [DNV-RP-F105, 2006]. In modern design codes, such as Det Norske Veritas' recommended practice provisions “Free Spanning Pipelines”, DNV-RP-F105 [2006], VIV is allowed in free span design as long as the designer can document that vibrations do not cause unacceptable fatigue damage or excessive bending moments. Hence, mode shapes and modal stresses are also important parameters since the stress ranges resulting from vibration must be part of fatigue assessments.

Semi-analytical, or simplified approximate solutions to determine modal frequencies and stresses in free spans is of significant interest to the pipeline industry, since pipelines are long and may often have hundreds or even thousands of free spans along their routes. Performing detailed finite element analyses (FEA) to determine response frequencies for hundreds of free spans or more is not attractive in terms of engineering efficiency, and may not even be feasible. As a result, the engineering community has historically sought simplified approximations to determine free span frequencies, based on idealized boundary conditions at span ends [Xiao and Zhao, 2010]. Vedeld et al. [2013] presented a fast semi-analytical solution for the prediction of frequencies and modal stresses in single spans with very high accuracy. The model of Vedeld et

al. [2013] is an improvement to existing semi-empirical solutions developed by Fyrileiv and Mørk [2002], increasing both range of validity and accuracy, and the model was later extended to consider pipeline double-spans on idealized flat seabeds [Sollund and Vedeld, 2013]. In their study, Sollund and Vedeld demonstrated that a semi-analytical solution is highly relevant for conducting parametric studies since computational efficiency of the semi-analytical solution is far superior to general purpose FEA (GPFEA) software. However, the semi-empirical solutions by Fyrileiv and Mørk [2002] and the semi-analytical solutions by Vedeld et al. [2013] are based on simplified static span configurations with flat span shoulders, constant effective axial force and static deflections only due to gravity. Other contributions to static deformation, such as axial feed-in caused by functional loading, are only included in an implicit manner through their effect on the input span lengths and effective axial force. Therefore, it is desirable to benchmark the approximate solutions against FEA solutions where seabed unevenness, variation in effective axial force and all relevant static loads are explicitly accounted for.

The main aim of the present report is to describe the implementation of, as well as to validate, a specific purpose FEA (SPFEA) tool for performing modal analyses of multi-span pipelines. The SPFEA tool will be based on a static pipe configuration determined by a state-of-the-art non-linear global FEA, accounting for geometric non-linearity, non-linear soil response and the load history. This non-linear global analysis, which in the context of pipeline design is performed to calculate static load effects for design checks and to establish free span lengths and gaps, is conventionally termed a "bottom roughness analysis" in the pipeline industry. The bottom roughness analyses, which thus will provide the input to the SPFEA solver, will be carried out using the GPFEA tool Abaqus [2012]. For completeness, and to facilitate understanding of important pipeline design aspects, the report will give descriptions of the bottom roughness and modal analyses procedures using Abaqus. The SPFEA solver will be thoroughly validated by comparisons to analytical results and to analyses using Abaqus. Based on the analyses using both FEA solvers, advantages and challenges with SPFEA and GPFEA solvers will be discussed. Finally, the report will investigate the effect of adopting continuous soil stiffness modeling rather than discrete springs, in addition to the effect of having different added mass coefficients in the axial and transverse directions.

# 2 PROBLEM DEFINITION

## 2.1 Basic Response Parameters

Figure 1 illustrates a free span, where the pipeline is suspended above the seabed between two touchdown points, conventionally termed span shoulders or soil supports. The figure also shows some of the basic parameters that govern the dynamic response of the pipeline, and these will be presented briefly in the following.

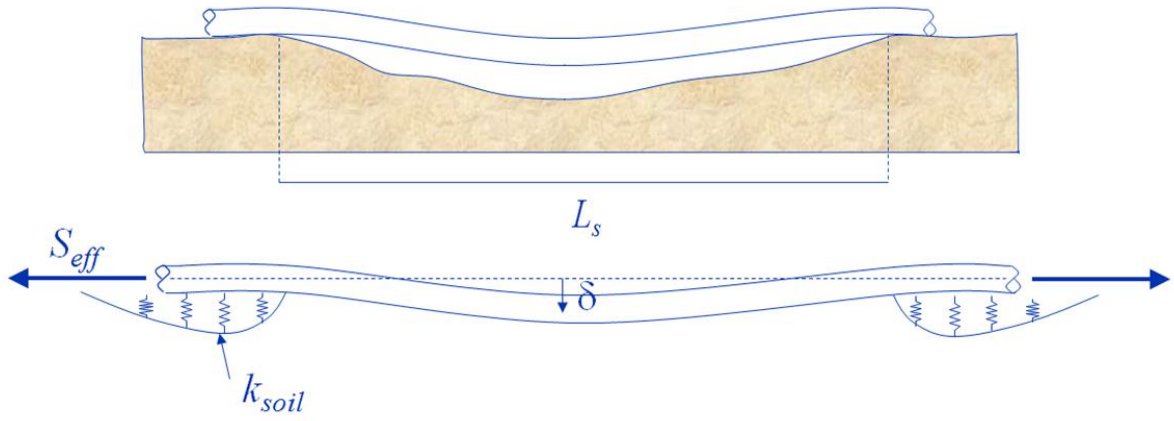


**Figure 1 – Pipeline free span, indicating free span length $L_s$ and mid-span deflection $\delta$. The figure is taken from Vedeld et al. [2013].**

Naturally, the dynamic response is strongly influenced by the span length, which is denoted $L_s$. The pipe has an effective mass $m_e$, which is taken as the sum of the dry mass, including the mass of the pipe steel and all coating layers, the mass of the fluid content and the hydrodynamic added mass (due to acceleration of the surrounding water). The bending stiffness of the pipe is $EI$, and the axial stiffness is $EA$, where $E$ is the Young's modulus, $I$ is the second moment of area and $A$ the cross-sectional area of the pipe steel. The stiffness properties of coating layers are normally disregarded, although the stiffening effect of concrete coating may be accounted for, if relevant [DNV-RP-F105, 2006].

As illustrated by Figure 1, pipe-soil interaction affects the modal response and must be adequately modeled. Linear elastic soil coefficients, given as $k_{soil}$ in the figure, are adopted in the SPFEA solver. It is distinguished between lateral, vertical and axial dynamic soil stiffness coefficients.

In addition to the structural stiffness and soil stiffness, the geometric stiffness of the pipeline must be accounted for. The geometric stiffness is governed by the effective axial force, indicated as $S_{eff}$ in Figure 1 [DNV-RP-F105, 2006; Vedeld et al., 2014]. The force is defined as positive in tension. It is equal to the axial force $N$ in the steel wall corrected for the effects of external pressure $p_e$ and internal pressure $p_i$, and is given by

$$S_{eff} = N - p_i A_i + p_e A_e \ , \qquad \textbf{(1)}$$

where $A_i$ is the internal cross-sectional area of the pipe, and $A_e$ the external cross-sectional area including all coating layers. Maximum compression is obtained for a pipe that is fully restrained axially, and the effective axial force may then be expressed as

$$S_{eff} = H_{eff} - \Delta p_i A_i (1 - 2\nu) - EA\alpha\Delta T \ , \qquad \textbf{(2)}$$

where $H_{eff}$ is the residual lay tension, $\Delta p_i$ is the change in internal pressure relative to internal pressure at the time of laying, $\alpha$ is the temperature expansion coefficient of the pipe steel and $\Delta T$ is the change in temperature from the time of laying. For a pipe that is completely unrestrained axially, the effective axial force is zero.

The soil stiffness is generally different in the lateral (in-line) and vertical (cross-flow) directions, and separate modal analyses must be carried out for the two directions. The dynamic response of the free span is also influenced by the static configuration of the pipeline. The static deflection into the span in the cross-flow direction causes a coupling between the bending stiffness and the axial stiffness of the pipe. This arc-like effect makes the pipe stiffer and may result in a significant increase of the natural frequency. Thus, the fundamental cross-flow frequency depends on the mid-span deflection $\delta$, as indicated in Figure 1. The static deflection is normally ignored in the in-line direction, but should be accounted for if the drag loading due to steady current is non-negligible.

### 2.2 Static Analysis

The SPFEA solver is designed to perform modal analyses only, and the static pipe geometry, effective axial force and the positions of nodes with pipe-soil contact are taken as input to the SPFEA solver. These quantities are determined by a preceding (static) bottom roughness analysis using the GPFEA software Abaqus. In order to facilitate a better and more complete

understanding of the free span design process, key aspects of the static analysis methodology will be outlined in the following. Details on the modeling in Abaqus will be given later in Section 4.1.

The static configuration of the pipeline, as well as the span lengths and effective axial forces, will vary between the different phases of the pipeline's design life, and free span assessments must consequently be performed separately for each phase. The following conditions must be considered:

- as-laid condition, which is the temporary phase right after installation, when the internal pressure and temperature typically are small and the effective axial force is equal to the residual lay tension. Since pipelines most often are empty in this phase and the effective axial force is tensile, the span lengths and gaps are expected to be large, and the static deflection due to self-weight is expected to be modest.
- flooded or water-filled condition, when the pipe is filled with water prior to the system pressure test. The increased submerged weight due to the water content will result in large static deflections due to gravity. The deflections into the spans cause a lengthening of the pipe and the effective axial force may thus obtain large tensile values in areas with many spans.
- pressure test condition, when the pressure in the water-filled pipe is increased to test level. The duration of the pressure test is so short that modal analyses and assessments of fatigue due to VIV are normally not required. However, because the static analysis is non-linear and dependent on the loading sequence, the pressure test should be included in the static analysis for an accurate estimation of the static configuration in subsequent phases.
- operating condition, which starts when the pipeline is filled with the intended fluid, e.g., oil or gas. It is, of course, the longest phase in the design life of the pipeline. When operational pressure and temperature are applied, the effective axial force becomes compressive, as seen from Eq. (2). The increased internal pressure and temperature cause the pipe to expand, slide axially and sag deeper into the spans (a process termed "feed-in"). Consequently, free span lengths and gaps tend to decrease in the operational phase.

- shut-down condition. The pipe may experience several cycles of alternating shut-down and operational conditions. If the duration of the shut-down phases is non-negligible with regard to fatigue damage, the static configuration must be determined also for shut-down conditions (i.e., with fluid content, but with reduced pressure and temperature).

Pipelines are long, slender structures, which are prone to large static displacements. Geometric non-linear effects are therefore important. In particular, relaxation of the effective axial force due to sagging into the spans, as described in detail by Fyrileiv et al. [2010] and Vedeld et al. [2013], must be accounted for in the static analysis. The seabed topography, such as the inclination and relative elevation of the span shoulders, influences the static deflections and the outcome of the static analysis as a whole (e.g., span lengths and effective axial force distribution). For this reason, the seabed surface is conventionally modeled based on survey data with high resolution, typically in the order of ~1 m.

The static analysis should also consider non-linear pipe-soil interaction in order to adequately model axial sliding effects and "feed-in". An elastic-plastic friction model may be applied, where the soil resistance is linear-elastic up to a specified "elastic slip" limit displacement. For displacements above this limit, the friction force may be taken as the product of a friction coefficient and the submerged pipe weight, according to a Coulomb friction model. In the present report, a two-dimensional model of the pipeline route is used. Consequently, only the axial friction coefficient is of importance. However, for analyses where lateral buckling and other three-dimensional effects are included, an anisotropic friction model with different friction coefficients in the axial and lateral directions is appropriate.

Naturally, the static pipe configuration also depends on the static vertical soil stiffness. The vertical pipe-soil interaction is also non-linear, in the sense that the stiffness is zero when there is a clearance between the pipe surface and the seabed, while typically a linear soil stiffness model is applied when the pipe penetrates into the soil.

From the description above, it should be noted that the submerged weight of the pipe (including its fluid content), the internal and external fluid pressure, thermal loads and lay tension constitute the functional loadings considered in the static analysis. Environmental loads are commonly disregarded, but loads from steady near-bottom currents should be included if they are

non-negligible. It should also be emphasized that the loading sequence may influence the results, and the bottom roughness analysis should therefore simulate the various phases that a pipeline goes through as accurately as possible.

### 2.3 Modal Analysis

The load effects due to VIV are usually calculated from empirically based response models. Separate response models for in-line and cross-flow VIV are provided in DNV-RP-F105 [2006]. The response models give the vibration amplitude as a function of the reduced velocity $V_R$, defined by

$$V_R = \frac{U_c + U_w}{f_n D}, \qquad \textbf{(3)}$$

where $U_c$ is the current velocity normal to the pipe, $U_w$ is the significant wave-induced flow velocity normal to the pipe, $D$ is the outer pipe diameter including any coating, and $f_n$ is the $n$-th eigenfrequency of the pipe in the relevant direction (in-line or cross-flow). Once the vibration amplitude is known, one may determine the stress range contributing to fatigue damage from the modal stress (i.e., the bending stress given by the mode shape) associated with the relevant eigenfrequency. Thus, for a reliable estimation of VIV fatigue, it is essential to determine eigenfrequencies and mode shapes with high accuracy.

The modal analysis, which will be performed by the SPFEA solver, solves the equation of motion for free vibrations of the pipe. It is a linearized procedure based on a tangent stiffness matrix, and the non-linear effects related to large displacements and pipe-soil interaction that were included in the static analysis are consequently ignored. The modal analysis must, however, account for the static equilibrium configuration since the system tangent stiffness matrix depends on the static curvature of the pipeline and the equilibrium level of effective axial force. The calculated response is thus strictly valid only for small vibrations [Kristiansen et al., 1998], but may, when used in conjunction with the empirically based response models in DNV-RP-F105, be applied for calculation of VIV fatigue damage also from larger-amplitude cross-flow oscillations.

As noted in Section 2.1, a linear soil stiffness model is applied with stiffness coefficients chosen according to the recommendations in DNV-RP-F105 [2006]. Different stiffness coefficients are used for the vertical, lateral and axial directions.

The mathematical formulation of the linearized eigenvalue problem will be given as part of the description of the SPFEA solver in Section 3, including explicit expressions for the mass matrix and the various contributions to the stiffness matrix. Damping is conventionally included in the VIV response models, and hence disregarded in the modal analysis.

### 2.4 Multi-Spans

On uneven seabeds the dynamic response of a particular free span may be affected by the presence of adjacent spans. In such cases it is necessary to introduce a multi-span model, where the modal analysis is carried out on a section of the pipeline that includes all the potentially interacting spans. An example of such a multi-span section, corresponding to a portion of the entire pipeline resting on a rough seabed, is presented in Figure 2. The pipeline stretch displayed in the figure is taken from an actual pipeline, with the seabed configuration obtained from survey measurements and the static equilibrium condition calculated by non-linear FEA.

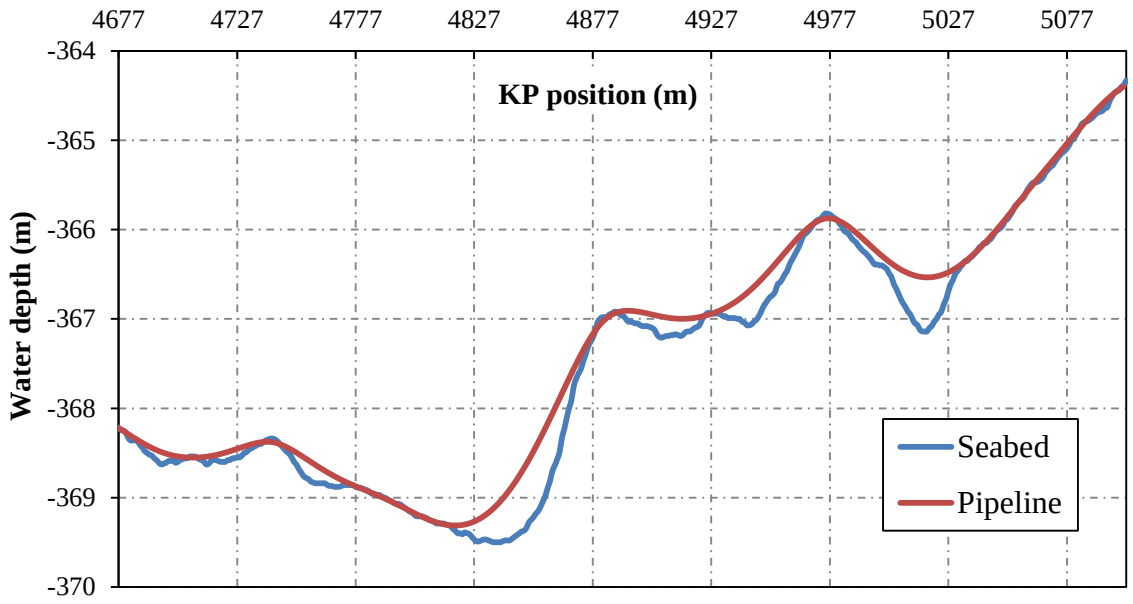


**Figure 2 – Multi-span section, corresponding to a portion of the entire pipeline where neighboring spans are sufficiently close that modal interaction may occur.**

It is difficult to assess when neighboring spans are interacting, and the current guidance given in DNV-RP-F105 for classification of free spans is inaccurate, as demonstrated by Sollund

and Vedeld [2013]. Since vortex-induced vibrations in the cross-flow direction are influenced by the curvature of the pipeline, it is of importance to study and establish the impact of actual rough seabed configurations on span interaction. The SPFEA solver that will be described in the present report is highly suited for such studies.

Since the static bottom roughness analyses are carried out on very long sections of the pipeline (ideally covering the entire pipeline in a single FE analysis), it may be argued that the modal analyses conveniently could be performed on the same long model. In that way, the complex interaction between spans would be accounted for, and the number of required modal analyses would be limited. There are, however, important reasons for limiting the length of each separate multi-span section. Single spans of similar length, but physically separated by a considerable distance, may have almost identical frequencies. In such cases, the FE analysis may due to numerical approximations or round-off errors present the two separate modes as a single interacting mode [DNV-RP-F105, 2006]. Furthermore, a large number of spans may respond simultaneously in a long FE model, even though several of the spans are located a long distance away from the span dominating the response. This has been explained as an artifact of the numerical modeling, since hydrodynamic damping and damping caused by friction is not accounted for in the modal analysis [Kristiansen et al., 1998]. Single spans that are incorrectly treated as interacting spans may lead to significant errors in the fatigue damage calculations. Thus, when using the SPFEA solver to analyze multi-spans, appropriate multi-span sections should be selected by manual inspection. Spans that are separated from the relevant multi-span by a long stretch of continuous pipe-soil contact should not be included in the analysis.

# 3 SPECIFIC PURPOSE FINITE ELEMENT ANALYSIS SOLVER

A specific purpose finite element analysis (SPFEA) solver has been implemented in a Matlab [2010] script, based on the methodology that will be described in the present section. In the SPFEA solver, the pipe is modeled as a planar Euler-Bernoulli beam, which implies that transverse shear deformation is disregarded and that the rotational inertia of the beam cross-section is assumed negligible compared to the translational inertia [Shames and Dym, 1991]. The loss of accuracy by ignoring these effects should, however, be almost negligible due to the high slenderness of the pipelines.

The SPFEA solver is designed to perform modal analyses for single- or multi-span pipelines based on the results of static bottom roughness analyses. The input required by the SPFEA solver is listed in Table 1. The final set of nodal coordinates from the static analysis is given as input to the SPFEA solver in the form of a double array called *Coords*(*i*,*j*). Since geometric non-linearity is accounted for in the static analysis, the element lengths $L_{el}$ vary along the pipeline and are calculated from the nodal coordinates.

**Table 1 – Input variables required by the specific purpose finite element solver.**

| Input variable | Unit | Description | Input variable | Unit | Description |
|---|---|---|---|---|---|
| $E$ | Pa | Young's modulus | *nNodes* | - | Number of nodes in pipe model |
| $D_s$ | m | Outer steel diameter | *nMod* | - | Number of modes to be calculated |
| $t_s$ | m | Pipe wall thickness | *Coords*(*i*,*j*) | m | Double array with *x*- and z-coordinates of pipe nodes |
| $m_{e,ax}$ | kg/m | Effective mass, axial direction | $k_v(i)$ | N/m/m | Vector with nodal values of vertical soil stiffness |
| $m_{e,tr}$ | kg/m | Effective mass, transverse direction | $k_l(i)$ | N/m/m | Vector with nodal values of lateral soil stiffness |
| $S_{eff}(i)$ | N | Vector with nodal values of effective axial force | $k_{ax}(i)$ | N/m/m | Vector with nodal values of axial soil stiffness |

In cases where the element resolution is refined as compared to the static analysis, new sets of nodal coordinates are obtained by linear interpolation. Similarly, linear interpolation between original nodal values is also applied to calculate new sets of the other input quantities given in the form of vectors, viz. effective axial force $S_{eff}(i)$ and soil stiffness coefficients $k_v(i)$, $k_l(i)$ and $k_{ax}(i)$.

The basic displacement assumption for an Euler-Bernoulli beam is given by [Shames and Dym, 1991]

$$u(x,y,t) = u_0(x,t) - y\frac{\partial v_0}{\partial x}(x,t), \qquad v(x,y,t) = v_0(x,t), \tag{4}$$

where $u_0$ and $v_0$ are the axial and transverse displacements of a point on the pipe centroidal axis. The $x$- and $y$-directions are indicated in Figure 3 along with the chosen convention for positive directions of the nodal degrees of freedom. Linear shape functions for the axial displacements and cubic displacements for the transverse displacements are applied, consistent with traditional Euler-Bernoulli finite element formulations [Bergan and Syvertsen, 1977; Cook et al., 2002; Shames and Dym, 1991]. Consequently, the shape function matrix **N** becomes

$$\mathbf{N}^T = \mathbf{N}_u^T + \mathbf{N}_v^T = \begin{bmatrix} 1-\dfrac{x}{L_{el}} & 0 \\ 0 & 2\left(\dfrac{x}{L_{el}}\right)^3 - 3\left(\dfrac{x}{L_{el}}\right)^2 + 1 \\ 0 & -x\left(1-\dfrac{x}{L_{el}}\right)^2 \\ \dfrac{x}{L_{el}} & 0 \\ 0 & -2\left(\dfrac{x}{L_{el}}\right)^3 + 3\left(\dfrac{x}{L_{el}}\right)^2 \\ 0 & \dfrac{x^2}{L_{el}}\left(1-\dfrac{x}{L_{el}}\right)^2 \end{bmatrix}, \tag{5}$$

where $\mathbf{N}_u$ is a matrix with $N_{u,11} = 1\text{-}(x/L_{el})$ and $N_{u,14} = x/L_{el}$ as its only non-zero entries, while $\mathbf{N}_v$ is a matrix with four non-zero entries corresponding to the standard shape functions for a beam. The displacement field for points on the centroidal axis of each element may then be expressed as

$$\mathbf{u}(x,t) = \begin{bmatrix} u_0(x,t) \\ v_0(x,t) \end{bmatrix} = \mathbf{N}\begin{bmatrix} u_1 & v_1 & \theta_1 & u_2 & v_2 & \theta_2 \end{bmatrix}^T = \mathbf{ND}. \tag{6}$$

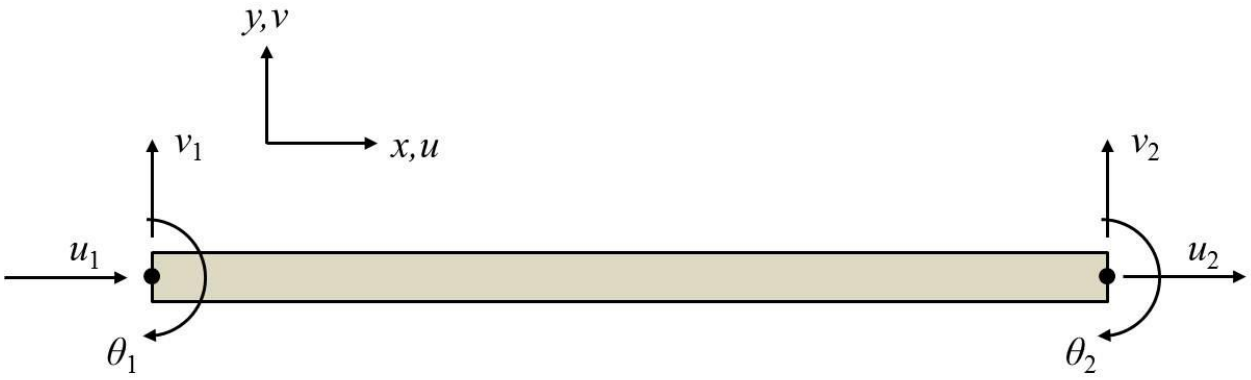


**Figure 3 – Element-local coordinate system and nodal degrees of freedom.**

As mentioned above, the rotational inertia of the pipe cross-section may be disregarded, and the kinetic energy may thus be represented by

$$T = \frac{1}{2}\int_0^{L_{el}} m_e \dot{\mathbf{u}}^T \dot{\mathbf{u}} dx = \frac{1}{2}\dot{\mathbf{D}}^T \left( \int_0^{L_{el}} m_e \mathbf{N}^T \mathbf{N} dx \right) \dot{\mathbf{D}}$$
$$= \frac{1}{2}\dot{\mathbf{D}}^T \left( \int_0^{L_{el}} \left( m_{e,ax} \mathbf{N}_u^T \mathbf{N}_u + m_{e,tr} \mathbf{N}_v^T \mathbf{N}_v \right) dx \right) \dot{\mathbf{D}} = \frac{1}{2}\dot{\mathbf{D}}^T \mathbf{M} \dot{\mathbf{D}} , \quad \textbf{(7)}$$

where a dot above the relevant variable denotes differentiation with respect to time, and where we have introduced the mass matrix **M**. As described in Section 2.1, $m_e$ denotes the effective mass per unit length, which comprises the total dry mass $m_d$ (i.e., the dry mass of the pipe steel, in addition to the dry mass from any liner, concrete coating or other coating layer) and the mass $m_{cont}$ of internal fluid content, as well as the added mass $m_a$ due to acceleration of the surrounding water particles:

$$m_e = m_d + m_{cont} + m_a \ . \quad \textbf{(8)}$$

The added mass contribution is calculated as

$$m_a = \frac{\pi}{4} C_a \rho_{water} D^2 \ , \quad \textbf{(9)}$$

where $C_a$ is the added mass coefficient, $\rho_{water}$ is the seawater density and $D$ again is the external diameter of the pipeline cross-section including all coating layers. The added mass coefficient for transverse displacements will generally be equal to unity for a free cylinder, but when the gap

between the pipe and the seabed becomes smaller than roughly a pipe diameter, $C_a$ will gradually increase to 2.29 as the gap is reduced to zero [DNV-RP-F105, 2006; Sumer and Fredsøe, 2006]. For axial displacements, on the other hand, it seems reasonable that the added mass coefficient must be close to zero, since almost no resistance from the surrounding water should be encountered when accelerating the pipe in the direction of the pipe axis. In the SPFEA solver, the effective mass $m_{e,ax}$ in the axial direction and $m_{e,tr}$ in the transverse direction are taken as input variables (see Table 1). Generally, $C_a$ will be taken as zero for calculation of $m_{e,ax}$ (except when the purpose of the calculations are direct comparison to GPFEA results, when a value of one will be used) and as one for calculation of $m_{e,tr}$. Thus, with reference to Eq. (7), $m_e$ will be set equal to $m_{e,ax}$ when calculating the entries $M_{11}$, $M_{14}$, $M_{41}$ and $M_{44}$ and equal to $m_{e,tr}$ for calculation of the remaining entries of the mass matrix **M**.

A consistent mass matrix, which has been implemented in the SPFEA solver, is obtained from Eq. (7) by carrying out the required integrations, resulting in the expression

$$\mathbf{M} = \frac{m_{e,tr} L_{el}}{420} \begin{bmatrix} 140\dfrac{m_{e,ax}}{m_{e,tr}} & 0 & 0 & 70\dfrac{m_{e,ax}}{m_{e,tr}} & 0 & 0 \\ 0 & 156 & -22L_{el} & 0 & 54 & 13L_{el} \\ 0 & -22L_{el} & 4L_{el}^2 & 0 & -13L_{el} & -3L_{el}^2 \\ 70\dfrac{m_{e,ax}}{m_{e,tr}} & 0 & 0 & 140\dfrac{m_{e,ax}}{m_{e,tr}} & 0 & 0 \\ 0 & 54 & -13L_{el} & 0 & 156 & 22L_{el} \\ 0 & 13L_{el} & -3L_{el}^2 & 0 & 22L_{el} & 4L_{el}^2 \end{bmatrix}. \qquad \textbf{(10)}$$

The total potential energy for a pipe element subject to free vibrations is given by [Bergan and Syvertsen, 1977; Cook et al., 2002; Vedeld et al., 2013]

$$\Pi = \frac{1}{2}\int_V E(\varepsilon_{xx})^2 \, dV + \frac{S_{eff}}{2}\int_0^{L_{el}} \left(\frac{\partial v_0}{\partial x}\right)^2 dx + \frac{1}{2}\int_0^{L_{el}} k_{soil}\mathbf{u}^T\mathbf{u}\, dx\,, \qquad \textbf{(11)}$$

where the first term represents elastic strain energy due to bending, the second term represents the work performed by the effective axial force $S_{eff}$ moving through the pipe lengthening caused by a transverse displacement $v_0$, and the third term represents the elastic strain energy in the soil.

From Eqs. (7) and (11) we may form the Lagrangian $L$ by

$$L = T - \Pi\,, \qquad \textbf{(12)}$$

and derive the equation of motion by applying Hamilton's principle

$$\delta \int_{t_0}^{t_1} (T - \Pi) dt = \delta \int_{t_0}^{t_1} L dt = 0 . \tag{13}$$

The equation of motion for free vibration becomes

$$\mathbf{M}\ddot{\mathbf{D}} + \mathbf{K}\mathbf{D} = \mathbf{0} , \tag{14}$$

where **M** is the mass matrix (defined by Eq. (7)), $\ddot{\mathbf{D}}$ is the acceleration vector, consisting of the second derivative with respect to time of the displacement vector **D**, and **K** is the total system stiffness matrix, given by

$$\mathbf{K} = \mathbf{K}_{struc} + \mathbf{K}_{g} + \mathbf{K}_{soil} . \tag{15}$$

From Eqs. (11) and (13), it may be deduced that the stiffness contribution associated with the elastic strain energy due to axial deformation and bending is given by the matrix

$$\mathbf{K}_{struc} = EA \int_0^{L_{el}} \mathbf{N}_{u,x}^T \mathbf{N}_{u,x} dx + EI \int_0^{L_{el}} \mathbf{N}_{v,xx}^T \mathbf{N}_{v,xx} dx . \tag{16}$$

Subscripts preceded by a comma are used here to denote partial differentiation. After carrying out the integrations, the structural stiffness matrix becomes [Bergan and Syvertsen, 1977; Cook et al., 2002]

$$\mathbf{K}_{struc} = \frac{2EI}{L_{el}^3} \begin{bmatrix} \frac{EA \cdot L_{el}^2}{2EI} & 0 & 0 & -\frac{EA \cdot L_{el}^2}{2EI} & 0 & 0 \\ 0 & 6 & -3L_{el} & 0 & -6 & -3L_{el} \\ 0 & -3L_{el} & 2L_{el}^2 & 0 & 3L_{el} & L_{el}^2 \\ -\frac{EA \cdot L_{el}^2}{2EI} & 0 & 0 & \frac{EA \cdot L_{el}^2}{2EI} & 0 & 0 \\ 0 & -6 & 3L_{el} & 0 & 6 & 3L_{el} \\ 0 & -3L_{el} & L_{el}^2 & 0 & 3L_{el} & 2L_{el}^2 \end{bmatrix} . \tag{17}$$

The geometric stiffness matrix, arising from the work of the effective axial force, is defined by [Bergan and Syvertsen, 1977; Cook et al., 2002]

$$\mathbf{K}_g = S_{eff}\int_0^{L_{el}} \mathbf{N}_{v,x}^T \mathbf{N}_{v,x}\, dx$$

$$= \frac{S_{eff}}{30L_{el}} \begin{bmatrix} 0 & 0 & 0 & 0 & 0 & 0 \\ 0 & 36 & -3L_{el} & 0 & -36 & -3L_{el} \\ 0 & -3L_{el} & 4L_{el}^2 & 0 & 3L_{el} & -L_{el}^2 \\ 0 & 0 & 0 & 0 & 0 & 0 \\ 0 & -36 & 3L_{el} & 0 & 36 & 3L_{el} \\ 0 & -3L_{el} & -L_{el}^2 & 0 & 3L_{el} & 4L_{el}^2 \end{bmatrix}. \qquad \textbf{(18)}$$

The final contribution to the stiffness matrix is due to the consistent soil stiffness matrix, which based on Eqs. (11) and (13), is found to be

$$\mathbf{K}_{soil} = \int_0^{L_{el}} \left( k_{ax} \mathbf{N}_u^T \mathbf{N}_u + k_{tr} \mathbf{N}_v^T \mathbf{N}_v \right) dx$$

$$= \frac{k_{tr} L_{el}}{420} \begin{bmatrix} 140\frac{k_{ax}}{k_{tr}} & 0 & 0 & 70\frac{k_{ax}}{k_{tr}} & 0 & 0 \\ 0 & 156 & -22L_{el} & 0 & 54 & 13L_{el} \\ 0 & -22L_{el} & 4L_{el}^2 & 0 & -13L_{el} & -3L_{el}^2 \\ 70\frac{k_{ax}}{k_{tr}} & 0 & 0 & 140\frac{k_{ax}}{k_{tr}} & 0 & 0 \\ 0 & 54 & -13L_{el} & 0 & 156 & 22L_{el} \\ 0 & 13L_{el} & -3L_{el}^2 & 0 & 22L_{el} & 4L_{el}^2 \end{bmatrix}. \qquad \textbf{(19)}$$

In Eq. (19), the transverse soil stiffness $k_{tr}$ is taken as the vertical dynamic soil stiffness $k_v$ when performing modal analyses in the cross-flow direction, while it is taken as the lateral dynamic soil stiffness $k_l$ when carrying out modal analyses in the in-line direction. It should also be noted, as mentioned previously, that the soil stiffness coefficients $k_v$, $k_l$ and $k_{ax}$ are given as input to the SPFEA solver in the form of vectors, with one value for each node. Consequently, the value assigned to pipe element number $i$ is given by

$$k_{tr,el}(i) = \frac{k_{tr}(i) + k_{tr}(i+1)}{2}, \qquad \textbf{(20)}$$

and in an identical manner for the axial soil stiffness. By giving the soil stiffness coefficients as vectorized input, it is straightforward to consider variation in soil properties along the multi-span model. In the free spans, the values of the soil stiffness coefficients are obviously zero.

A consistent soil stiffness element, as given by Eq. (19), is not available in the GPFEA sotware Abaqus, which will be used for validation of the SPFEA solver. Instead a lumped formulation must be used, where linear springs are applied for modeling of the soil stiffness. In order to enable direct comparison with Abaqus results, an option for a similar modeling of soil stiffness has been included in the SPFEA solver. The stiffness matrix for a linear spring is defined by [Cook et al., 2002]

$$\mathbf{K}_{spring} = k_{tr} L_{el} \begin{bmatrix} 1 & -1 \\ -1 & 1 \end{bmatrix}. \qquad \textbf{(21)}$$

The definition is of course identical for an axial spring, with $k_{tr}$ replaced by $k_{ax}$. Note that the stiffness matrix in Eq. (21) relates to the degrees of freedom of the spring, only one of which is shared with the pipe elements. After implementation of boundary conditions, the resulting contribution to the pipe stiffness matrix **K** is therefore an addition of $k_{tr}L_{el}$, or alternatively $k_{ax}L_{el}$, to the diagonal entry of **K** which corresponds to the relevant degree of freedom ($u_i$ or $v_i$). Hence, the main differences from the consistent formulation, Eq. (19), are the lack of rotational stiffness and that there are no terms with coupling between translational and rotational degrees of freedom. For high element resolutions this should normally entail a negligible loss of accuracy, but for very rough seabeds with short intermediate shoulders in-between spans, the effect may be non-negligible even for a very refined element mesh. Such effects will be studied in some detail in Section 6.5.

Since a pipeline is a one-dimensional structure, effectively modeled as a single, long beam with varying contribution from soil stiffness along its length, the element assembly process is straight-forward with no need for the use of e.g., topology matrices. However, because the elements are rotated relative to each other, the local mass and stiffness matrices for each element must be transformed to relate to a global coordinate system, rather than to the element-local coordinate system. The coordinate systems are illustrated in Figure 4, and the mass and stiffness relations are transformed to global coordinates by performing the similarity transformations

$$\mathbf{M}_{gc}(i) = \mathbf{T}^T \mathbf{M}(i) \mathbf{T} \quad \text{and} \quad \mathbf{K}_{gc}(i) = \mathbf{T}^T \mathbf{K}(i) \mathbf{T} \qquad \textbf{(22)}$$

prior to element assembly [Bergan and Syvertsen, 1977; Cook et al., 2002]. In Eq. (22), the subscripts "*gc*" indicates that the matrices are expressed in the global coordinate system. The matrices **M**(*i*) and **K**(*i*) are the mass and stiffness matrices in the local coordinate system, as

given by Eqs. (10) and (15), with the index *i* indicating that they belong to element number *i*. The rotation matrix **T** is given by

$$\mathbf{T} = \begin{bmatrix} \cos\theta & \sin\theta & 0 & 0 & 0 & 0 \\ -\sin\theta & \cos\theta & 0 & 0 & 0 & 0 \\ 0 & 0 & 1 & 0 & 0 & 0 \\ 0 & 0 & 0 & \cos\theta & \sin\theta & 0 \\ 0 & 0 & 0 & -\sin\theta & \cos\theta & 0 \\ 0 & 0 & 0 & 0 & 0 & 1 \end{bmatrix}, \qquad \textbf{(23)}$$

where for each element the rotation angle $\theta$ is calculated from the static configuration given by the *Coords*(*i*,*j*) array.

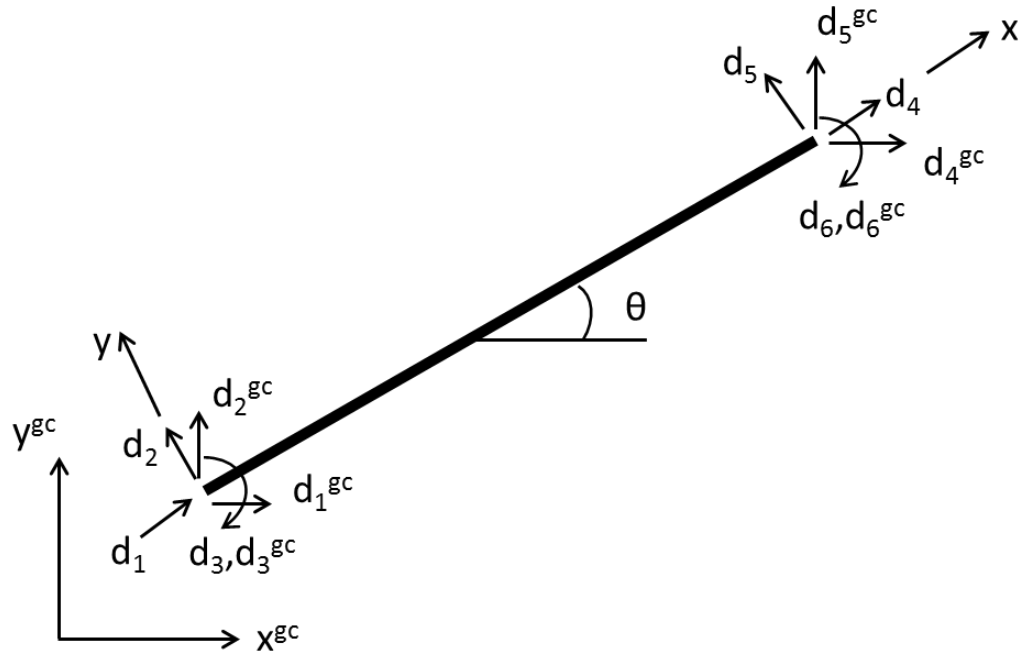


**Figure 4 – Nodal degrees of freedom in the local ($d_i$) and the global ($d_i^{gc}$) coordinate systems.**

The element assembly is then easily performed according to the direct stiffness method by [Cook et al., 2002]

$$\mathbf{M}_{glob} = \sum_i \mathbf{M}_{gc}(i) = \sum_i \mathbf{T}^T \mathbf{M}(i)\mathbf{T} \quad \text{and} \quad \mathbf{K}_{glob} = \sum_i \mathbf{K}_{gc}(i) = \sum_i \mathbf{T}^T \mathbf{K}(i)\mathbf{T}, \qquad \textbf{(24)}$$

where it is assumed that the element matrices have been expanded in the trivial manner to match the dimensions of the global mass matrix $\mathbf{M}_{glob}$ and stiffness matrix $\mathbf{K}_{glob}$. In Matlab code this may be achieved through the simple algorithm below:

```
M_glob=zeros(3*nNodes, 3*nNodes);
K_glob=zeros(3*nNodes, 3*nNodes);

r=1;

for i=1:nNodes-1
      M_glob(r:r+5,r:r+5)= M_glob(r:r+5,r:r+5)+M_gc(i);
      K_glob(r:r+5,r:r+5)= K_glob(r:r+5,r:r+5)+K_gc(i);
      r = r+3;
end
```

After the assembly process has been carried out, boundary conditions may be implemented in the conventional manner by removing rows and columns of the augmented matrices that are related to the relevant degrees of freedom [Cook et al., 2002]. In the SPFEA solver, the boundary conditions were taken as pinned-pinned, i.e., the translational degrees of freedom ($u_1$, $v_1$, $u_{nNodes}$, $v_{nNodes}$) were suppressed, while the rotational degrees of freedom ($\theta_1$, $\theta_{nNodes}$) were retained, at both pipe ends. All mass and stiffness coefficients related to the suppressed degrees of freedom were omitted already prior to assembly, consistent with the direct stiffness method [Cook et al., 2002]. Simply supported ends were chosen in order to align the SPFEA solver with the boundary conditions in the semi-analytical method developed by Vedeld et al. [2013], but the solver could of course easily be modified to consider other sets of boundary conditions.

With regard to soil modeling, it is not obvious whether the soil stiffness contributions to the stiffness matrix should be rotated in the same manner as the other stiffness terms. In the Abaqus model, the axial and transverse soil springs relate directly to the global coordinates, i.e., if the pipeline element is rotated relative to the global *x*-axis, the axial soil stiffness will in practice contribute with both a tangential and a normal stiffness component. Similarly, the transverse soil stiffness will give rise to an axial component, as well as to a transverse component. In order to align the analyses performed with the SPFEA solver to the Abaqus analyses, the soil stiffness is

added to the global stiffness matrix in the same manner when the soil is modeled using linear springs (Eq. (21)). However, when using the consistent formulation, Eq. (19), the local soil stiffness matrices $\mathbf{K}_{soil}$ are transformed to global coordinates by performing the similarity transformation described by Eq. (22). Consequently, the axial soil stiffness will keep acting as a purely tangential resistance to pipe displacements, and the transverse soil stiffness will act solely in the direction normal to the pipe axis.

# 4 GENERAL PURPOSE FINITE ELEMENT ANALYSIS

## 4.1 Static Analysis

The modal analysis carried out by the SPFEA solver is based on a static equilibrium configuration determined by a preceding static analysis. The static analysis is often referred to as a bottom roughness analysis in the pipeline engineering community, and the analysis methodology was outlined in Section 2.2. In the present work, the bottom roughness analyses are performed using the general purpose finite element analysis (GPFEA) tool Abaqus [2012]. The Abaqus modeling will be described in more detail in the following.

The pipeline is modeled using PIPE31H elements. PIPE31H elements are first order shear deformable 3D hybrid beam elements based on Timoshenko beam theory [Shames and Dym, 1991], with an additional formulation to distinguish between effective and true wall axial forces. The hybrid property (indicated by the "H" in the element name) implies that the elements use a formulation in which the axial and transverse shear forces in the elements are included as primary variables, in addition to the nodal displacements and rotations. The hybrid beam element formulation is advantageous in geometrically nonlinear analysis for beams that undergo very large rotations, but are quite rigid in axial and transverse shear deformation (e.g., for offshore pipelines and cables). Although hybrid beam elements are computationally more expensive, they generally converge much faster when the beam's rotations are large, thereby being more efficient overall in such cases [Abaqus, 2012].

The PIPE-element library in Abaqus is assigned a beam section of type "pipe" by default, implying that the cross-section is modeled as a single-layer hollow cylinder. Coating layers, i.e. thermal insulation, paint, adhesives, corrosion protection, concrete coating or combinations thereof, are assumed not to contribute with any stiffness. However, their impact on the dry mass and buoyancy are included in the models.

The seabed is modeled using the surface elements R3D4. The seabed elements are generated based on the survey data input, and they are assigned nodal coordinates corresponding to their actual locations. A contact pair is generated between the pipe elements and the seabed surface, and the contact is modeled using normal and tangential stiffness based on a static vertical soil stiffness coefficient and friction coefficients for the lateral and axial directions. Element resolution is taken equal to the survey data resolution (typically ~1 m in axial direction) for both

the pipeline and seabed elements. Having equal resolution enhances analysis stability since initial contact between the surfaces is node-to-element boundary. Typical model lengths are between 6 and 24 km. Pipelines that are longer than the indicated model length interval are sectioned. In order to ensure proper boundary behavior between pipe sections, the sections overlap. Suitable overlap lengths are determined by requiring convergence of the effective axial force between the overlapping sections.

In Section 2.2, it was described that the outcome of the static analysis depends on the load history and that the static equilibrium configuration should be determined for each distinct phase of the pipeline's design life (e.g., for as-laid conditions, water-filled conditions and operational conditions). For this reason, the analysis is typically divided into a series of load steps that are meant to represent the various phases that a pipeline goes through. A typical bottom roughness analysis comprises the following steps:

1. Gravity and buoyancy are introduced.
2. The pipe is laid down on the seabed.
3. The effective lay tension is applied.
4. Seabed friction is activated.
5. The pipe is filled with water.
6. Pressure is increased to model the pressure test.
7. Pressure is removed to model the end of the pressure test.
8. Operational temperature, pressure and content are introduced.
9. A number of shut-down cycles may be modeled, in which operational temperature and pressure are removed and re-introduced.

Initially, the pipe elements are generated in a straight line with z-coordinate equal to the highest point on the seabed, as visualized in Figure 5.

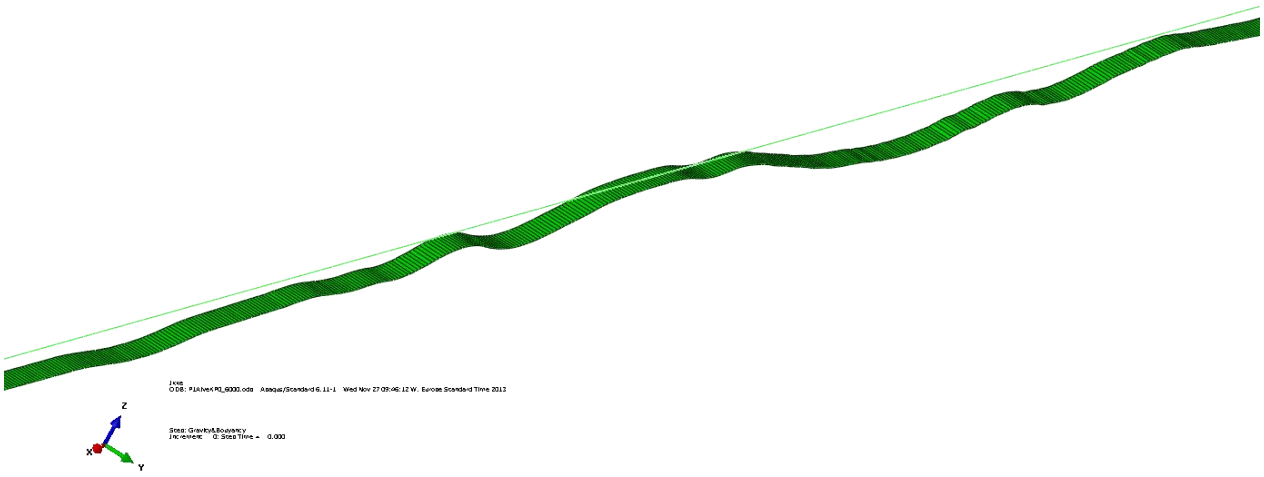

**Figure 5 – Seabed and initial pipeline configuration prior to introduction of gravity and buoyancy.**

Subsequently, gravity and buoyancy are introduced to the model, and the pipe is laid down on the seabed making use of stabilizing measures as detailed by Aamlid and Røneid [2008]. After contact has been established between the pipe and the seabed, friction behavior between the pipe and seabed is deactivated. One end node is fixated, and the effective lay tension is applied at the other. When the effective lay tension is approximately constant over the length of the pipe, the seabed friction behavior is reactivated and the pipe is regarded as in the "as-laid" condition. An example of the nearly uniform effective axial force distribution in the as-laid condition is shown in Figure 6.

In Figure 6, the pipeline is shown resting on the seabed. It is observed from the figure that the effective axial force varies approximately ± 2.5% about the mean value of 200 kN. The value of 200 kN was the input effective lay tension to the analysis, which in this case illustrates that the methodology is fairly accurate in establishing the as-laid condition.

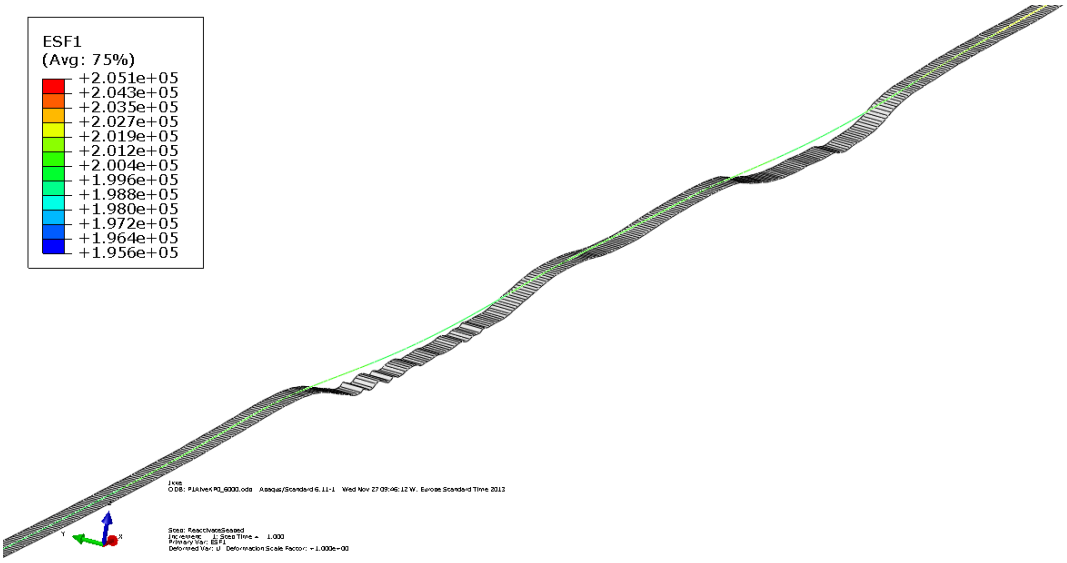


**Figure 6 – Pipeline in as-laid condition, showing a nearly uniform effective axial force distribution.**

After the as-laid condition, the pipe is filled with water. The water-filling process is conducted in order to perform the system pressure test, which is the next step in the analysis. As indicated in Section 2.2, it is not necessary to perform modal analysis for the system pressure test condition (because its duration is very short and may thus be disregarded with respect to fatigue utilization). However, the pipe-soil contact and axial feed-in into free spans are non-linear effects, which means the system pressure test condition may influence on the static configuration in the operational condition. Therefore, it is included in the static analyses even if not directly relevant as a separate stage in the dynamic analyses.

Finally, the operational condition is modeled by introducing operational temperature, content weight and pressure. The area previously shown in Figure 6 is shown again in Figure 7 for the operational condition. As expected from Eq. (2), the effective axial force becomes compressive in this phase.

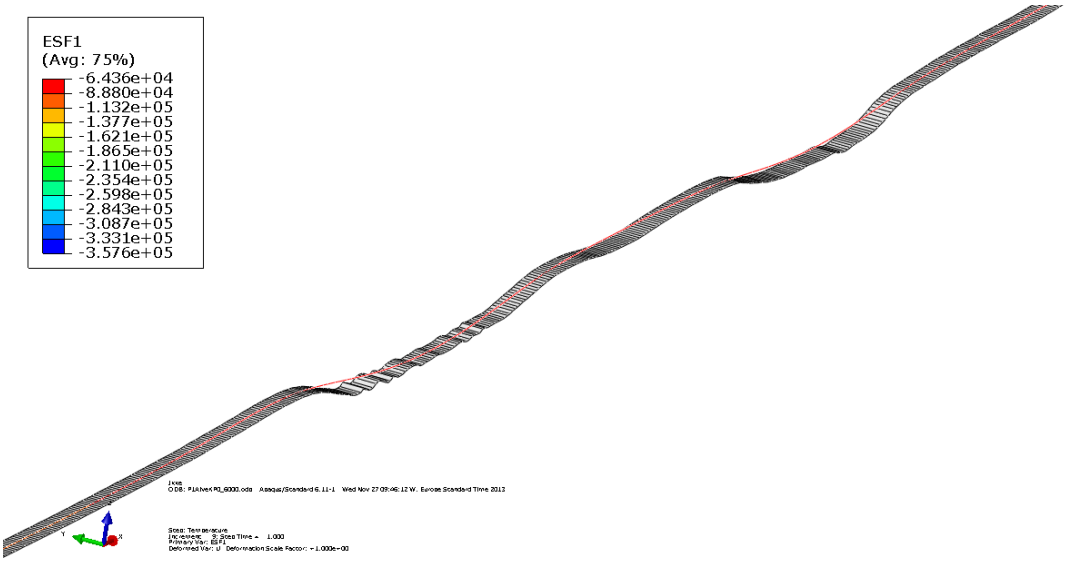


**Figure 7 – Pipeline in operational condition, showing compressive effective axial forces.**

In all the steps of the static analysis, the NLGEOM option in Abaqus is turned on, implying that geometric non-linearities are accounted for. Thus, the elements are, in each increment of each step of the analysis, based on the current deformed configuration using current nodal positions. Consequently, element lengths are continuously updated, and changes in the effective axial force as a result of static deflections are accounted for.

## 4.2 Modal Analysis

The SPFEA solver presented in Section 3 will be validated by comparison to modal analyses performed with the GPFEA software Abaqus [2012]. The modal analysis procedure in Abaqus will be described in the following.

When the static configuration has been determined according to the analysis methodology described in the preceding section, contact information is extracted from Abaqus for every pipeline node, along with nodal coordinates and the effective axial force in each pipe element. In Abaqus, whenever a contact pair has been established (such as the contact between the pipe surface and the seabed in the present context), the nodal variable COPEN contains the contact opening at the surface nodes. Thus, by extracting the value of COPEN for each pipeline node, the gap between the pipe and the seabed is obtained. A negative value for COPEN implies that the

pipe has penetrated the seabed, while a positive value indicates that the pipe is in a span. By inspection of the static pipe configuration and the distribution of corresponding gaps, the modeled pipe is divided into relevant multi-span sections, as described in Section 2.4. An example of a multi-span section and a corresponding gap distribution is shown in Figure 8.

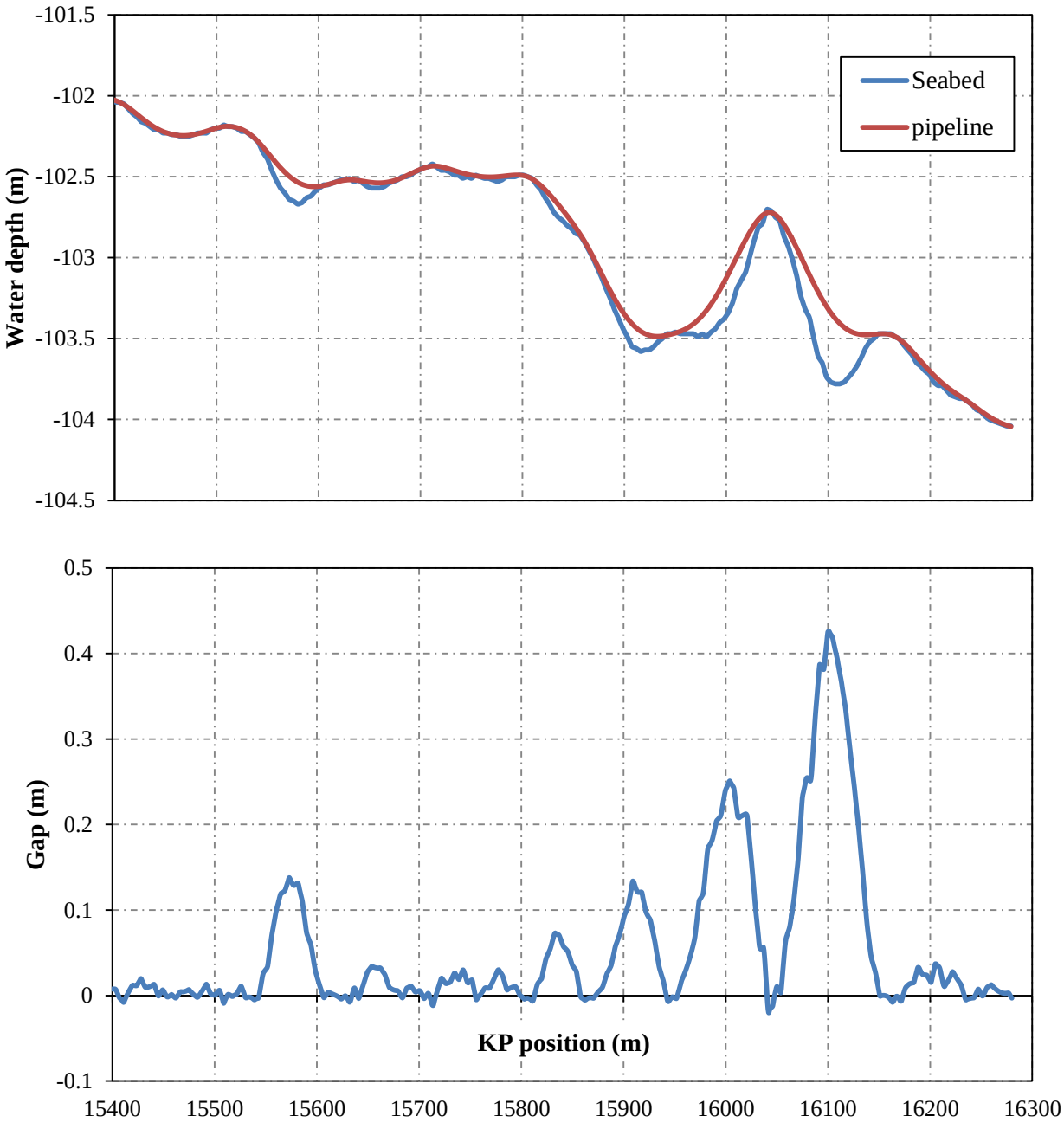


**Figure 8 – Static pipeline configuration (above) and gap between the seabed and the pipe (below).**

For each multi-span section, a new contact pair is defined between the pipe and the seabed surface elements, and intermediate pipe sections between multi-span sections are also assigned individual contact pair definitions. The pipe elements are sectioned into new element sets, corresponding to the new contact pair definitions. Sets of dynamic springs to model axial, lateral and vertical pipe-soil stiffness are defined, with stiffness coefficients taken according to DNV-RP-F105 [2006]. In vertical direction, the static vertical stiffness between the pipe and the seabed must be subtracted from the vertical dynamic spring stiffness. The new dynamic spring nodes and contact pair definitions, which are introduced based on the contact results from the static analyses, are not permissible to introduce using the "restart" functionality in Abaqus. Hence, the full static analysis must be re-run including the new dynamic soil stiffness springs and contact pair definitions. Once the dynamic springs have been defined in the second static analysis, they are deactivated until they are reintroduced prior to performing the relevant modal analysis.

After completing the second static analysis, modal analyses may be conducted for each multi-span section, in each phase, by restarting the analysis in the relevant phase. There are two individual steps in the modal analysis:

1. Vertical, axial and lateral dynamic springs are reactivated in the model (strain free). At each end of the pipeline element set corresponding to the relevant multi-span section, the nodes are fixed in translational degrees of freedom (pinned) and in rotation around the pipe axis. Friction is deactivated in axial and lateral directions. All pipe element sets and contact pairs which are not associated with the relevant multi-span section are removed from the model.
2. Pipe added mass is included and modal analysis is conducted.

# 5 CASE STUDY DESCRIPTIONS

## 5.1 Simply Supported Beam Model

The dynamic response of an axially loaded, simply supported beam with no static deformation is studied first. Using the same model, a static deformation due to a compressive effective axial force and submerged weight is then introduced, and the static configuration obtained by the GPFEA solver is transferred into the SPFEA solver for subsequent modal analysis. For both comparative studies, a pipe with the properties described in Table 2 is used.

**Table 2 – Pipe and span properties for the simply supported beam model.**

| $D_s$ (m) | $t_s$ (m) | $E$ (GPa) | $S_{eff}$ (kN) | $L_s$ (m) | $w_s$ (N/m) | $m_e$ (kg/m) |
|---|---|---|---|---|---|---|
| 0.1683 | 0.0151 | 207 | -45 | 15 | 335.5 | 79.9 |

In Table 2, $D_s$ is the outer steel wall diameter, $t_s$ is the steel wall thickness and $w_s$ is the submerged weight.

In Abaqus, the case is modeled using PIPE31H elements. In addition, analyses are performed using the general beam element B33. In all the FE analyses, 100 elements were used, corresponding to an element length of slightly less than one pipe diameter. The PIPE31H element is described in Section 4.1 of this document. The B33 element is a 3D Euler-Bernoulli beam element, directly comparable to the element formulation for the SPFEA solver described in Section 3.

The modal response for a beam with simple pinned-pinned boundary conditions has a well-known analytical solution:

$$f_i = \frac{\pi i^2}{2L_s^2}\sqrt{\frac{EI}{m_e}\left(1+\frac{S_{eff}}{EI}\left(\frac{L_s}{i\pi}\right)^2\right)} \qquad \textbf{(25)}$$

where $i$ is the mode number. For the simple pinned-pinned boundary condition, both FEA solvers will therefore be compared to the analytical solution given by Eq. (25).

### 5.2 Single Free Span on a Flat Seabed

A single free span on an idealized flat seabed is studied next. A physical description of how the free span and seabed are modeled is given in Figure 9.

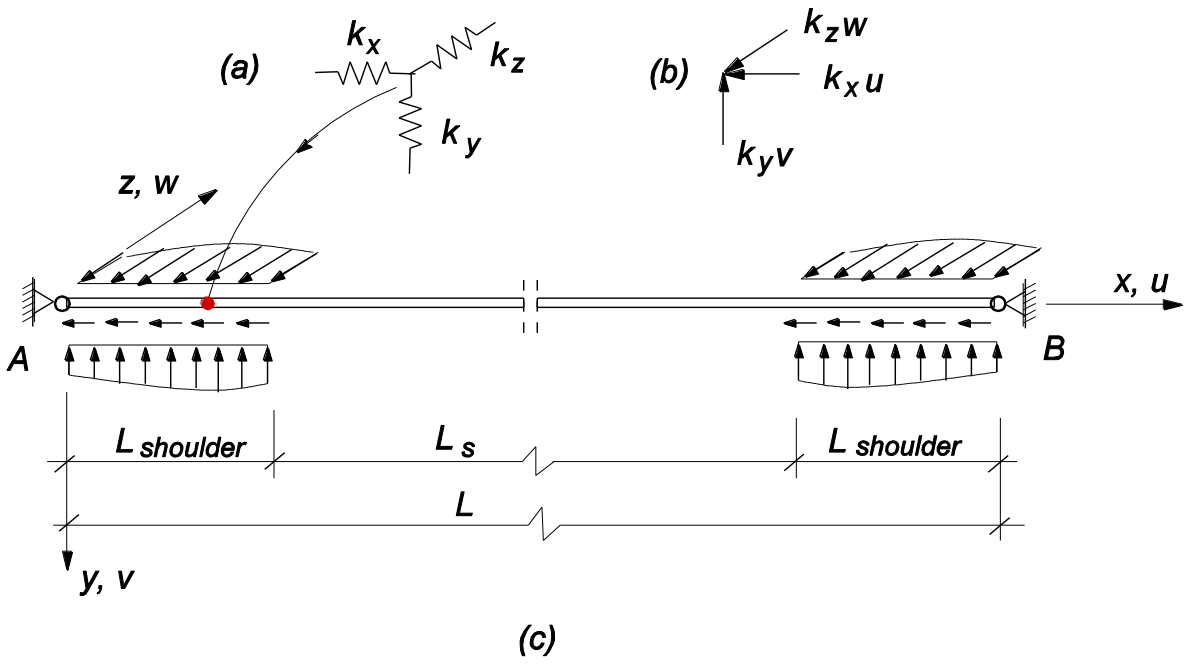


**Figure 9 –Definition of pipeline model and Cartesian coordinate system. (a) Static and dynamic soil springs are applied axially, laterally and vertically at the span shoulders. (b) Directions of spring forces. (c) Idealized free span model with boundary conditions. The figure is taken from Vedeld et al. [2013].**

The span length $L_s$ is set to 56.616 m. The element length is 0.07202 m and the shoulders on each side of the span are equal in length to the span length, i.e., the total model length $L = 3L_s$. A uniform effective axial force of -100 kN is applied. The pipe geometry, which is detailed in Table 3, is representative for a large-diameter, concrete-coated gas export pipe. The static deflection due to the combined action of the submerged weight and effective axial force is calculated in Abaqus, while modal analyses are carried out using both Abaqus (with PIPE31H and B33 elements) and the SPFEA solver.

**Table 3 – Pipeline geometry.**

| Variable | Symbol | Unit | Value |
|---|---|---|---|
| Steel wall outer diameter | $D_s$ | mm | 720.2 |
| Steel wall thickness | $t_s$ | mm | 20.1 |
| Corrosion coating | $t_{coat,1}$ | mm | 5 |
| Concrete coating | $t_{conc}$ | mm | 60 |

Relevant material properties for the steel wall section and densities for the corrosion coating and concrete are presented in Table 4. The pipeline is assumed to be in the as-laid phase, implying that there is no weight contribution from the content.

**Table 4 – Material data.**

| Variable | Symbol | Unit | Value |
|---|---|---|---|
| Steel Young's modulus | $E$ | GPa | 207 |
| Thermal expansion coefficient of steel | $\alpha$ | $°C^{-1}$ | $1.3 \cdot 10^{-5}$ |
| Poisson's ratio of steel | $\nu$ | - | 0.3 |
| Density of steel | $\rho_{steel}$ | $kg/m^3$ | 7850 |
| Density of corrosion coating | $\rho_{coat,1}$ | | 1300 |
| Density of concrete coating | $\rho_{conc}$ | | 2250 |

Seabed properties for the idealized shoulders are presented in Table 8. The same seabed properties apply for the entire length of the pipeline model. Note that the static axial stiffness is disregarded.

**Table 5 – Seabed geotechnical properties.**

| Variable | Symbol | Unit | Value |
|---|---|---|---|
| Static vertical stiffness | $k_{v,s}$ | $MN/m^2$ | 1.35 |
| Dynamic vertical stiffness | $k_v$ | | 35.5 |
| Dynamic lateral stiffness | $k_l$ | | 26.7 |
| Dynamic axial stiffness | $k_{ax}$ | | 26.7 |

The semi-empirical model of Fyrileiv and Mørk [2005], which is currently included in the recommended practice DNV-RP-F105 [2006], predicts in-line and cross-flow frequencies for single spans on the seabed with high accuracy [Sollund and Vedeld, 2012; Vedeld et al., 2013]. Therefore, the following equation will be applied to check the fundamental frequency $f_0$ calculated by the two FE models:

$$f_0 = 3.56\sqrt{\frac{EI}{m_e L_{eff}^4}\left(1+\frac{S_{eff}}{P_{cr}}+0.4\left(\frac{\delta}{D}\right)^2\right)}, \qquad \textbf{(26)}$$

where $L_{eff}$ is the effective span length, $P_{cr}$ is the critical buckling load and $\delta$ as previously is the static mid-span deflection (details on how to calculate these quantities may be found in Fyrileiv and Mørk [2002] or in DNV-RP-F105[2006]). For the in-line frequency calculation, the mid-span deflection is assumed equal to zero.

### 5.3 Multi-Span Section on Realistic Seabed – Case 1

A realistic seabed profile, taken from a field measurement survey, is shown below in Figure 10. The figure displays a 6-km section of a 15.7 km long gas pipeline route.

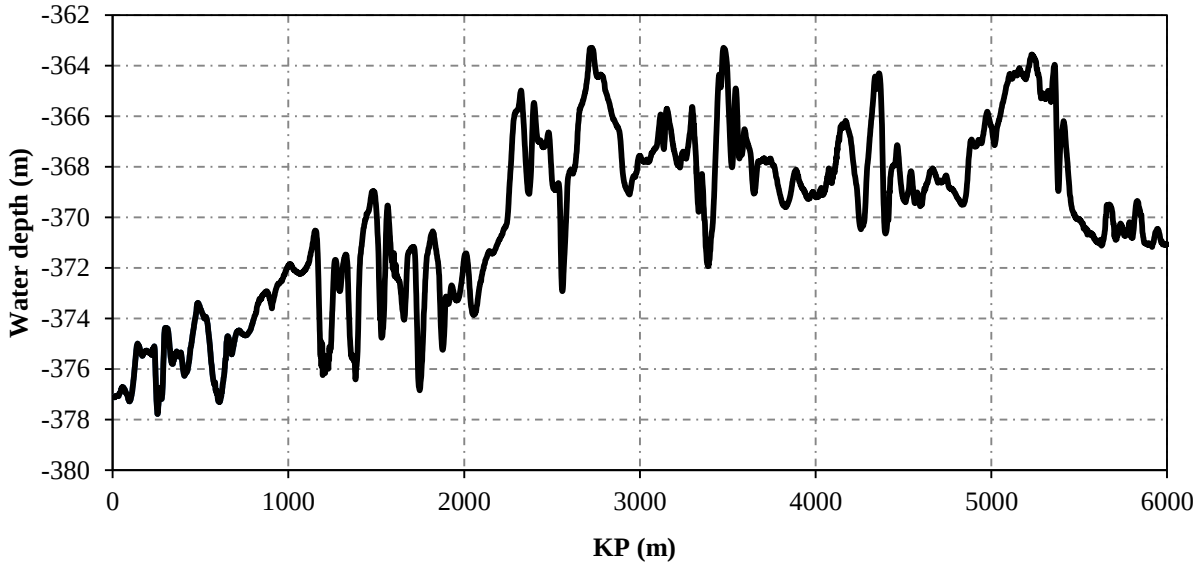


**Figure 10 – Seabed profile showing water depth as a function of kilometer point (KP).**

A small part of the 6-km seabed profile will be analyzed as a multi-span section. Based on results from a static analysis, carried out as described in Section 4.1, a multi-span section (later referred to as "multi-span section 1") is identified between KP 2100 and KP 2850. The relevant multi-span section is shown in Figure 11, where the static pipeline configuration in the operational phase is displayed along with the seabed profile.

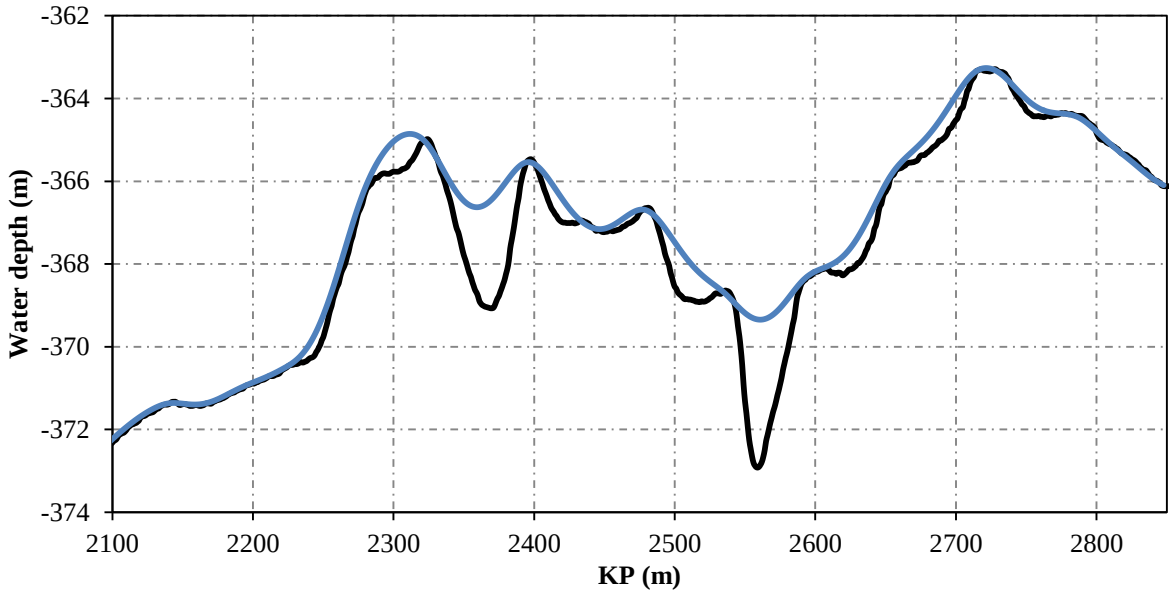


**Figure 11 – Seabed (black) and static pipeline configuration (blue) in operational condition as a function of KP for multi-span section 1.**

It is observed from the figure that there is fairly uniform contact between pipe and seabed near each end of the multi-span section, indicating that the pipeline stretch is chosen reasonably and that interaction with other spans outside the multi-span section is not to be expected. The pipeline geometry is specified in Table 6.

**Table 6 – Pipe geometry.**

| Variable | Symbol | Unit | Value |
|---|---|---|---|
| Steel wall outer diameter | $D_s$ | mm | 368 |
| Steel wall thickness | $t_s$ | mm | 24 |
| Epoxy primer | $t_{coat,1}$ | mm | 0.3 |
| Adhesive PP | $t_{coat,2}$ | mm | 0.3 |
| Solid PP | $t_{coat,3}$ | mm | 6.4 |
| PP foam | $t_{coat,4}$ | mm | 56.7 |
| Solid PP (Shield) | $t_{coat,5}$ | mm | 4 |

Stresses caused by thermal expansion and differences in Poisson's ratios of the coating systems compared to the steel wall, and resulting variations in the effective axial force [Vedeld et al., 2014], are disregarded. Relevant material properties for the pipe steel wall and densities for the coating systems are presented in Table 7.

**Table 7 – Material data.**

| Variable | Symbol | Unit | Value |
|---|---|---|---|
| Steel Young's modulus | $E$ | GPa | 207 |
| Thermal expansion coefficient of steel | $\alpha$ | $°C^{-1}$ | $1.3 \cdot 10^{-5}$ |
| Poisson's ratio of steel | $\nu$ | - | 0.3 |
| Density of steel | $\rho_{steel}$ | $kg/m^3$ | 7850 |
| Density of epoxy primer | $\rho_{coat,1}$ | | 1300 |
| Density of adhesive PP | $\rho_{coat,2}$ | | 900 |
| Density of solid PP | $\rho_{coat,3}$ | | 900 |
| Density of PP foam | $\rho_{coat,4}$ | | 600 |
| Solid PP shield | $\rho_{coat,5}$ | | 900 |
| Content density | $\rho_{cont}$ | | 200 |

Seabed properties for the route are presented in Table 8. The same seabed properties apply for the entire length of the multi-span section.

**Table 8 – Seabed geotechnical properties.**

| Variable | Symbol | Unit | Value |
|---|---|---|---|
| Static vertical stiffness | $k_{v,s}$ | $kN/m^2$ | 200 |
| Axial friction coefficient | $\mu_{ax}$ | - | 0.107 |
| Lateral friction coefficient | $\mu_l$ | - | 0.285 |
| Dynamic vertical stiffness | $k_v$ | $kN/m^2$ | 2293 |
| Dynamic lateral stiffness | $k_l$ | | 1567 |
| Dynamic axial stiffness | $k_{ax}$ | | 1567 |

In both the static and dynamic analyses, PIPE31H elements with element lengths of 1 meter are used in the GPFEA. Element lengths in the SPFEA are calculated based on the input nodal coordinates, as described in Section 3.

### 5.4 Multi-Span Section on Realistic Seabed – Case 2

The next case is based on a 3.7-km gas flowline in the Norwegian Sea. The seabed profile for the pipe corridor has been recorded in survey, and is shown below in Figure 12. This particular pipeline example is chosen because the seabed is very rough and the pipe submerged weight is very low. Consequently, the pipe has little contact with the seabed, and intermediate span shoulders are often minimal in length.

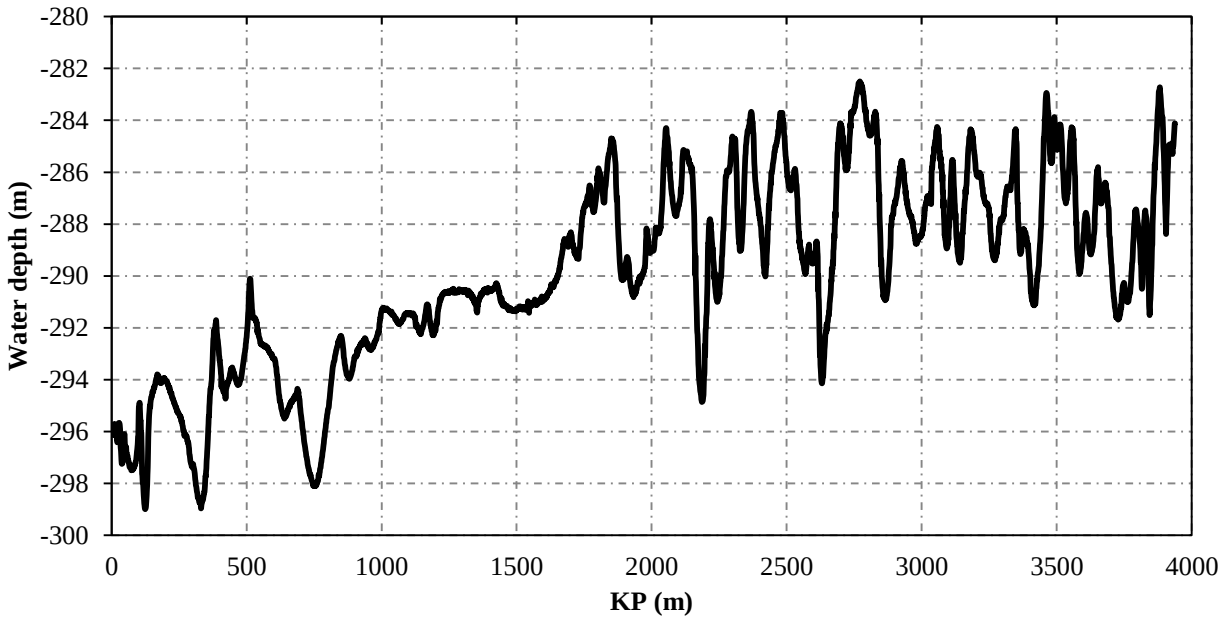


**Figure 12 – Seabed profile showing water depth as a function of kilometer point (KP).**

A portion of the 3.7-km pipeline route will be analyzed as a multi-span section. Based on results from a bottom roughness analysis, a multi-span section (multi-span section 2) is identified between KP 1543 and KP 3011. The seabed profile of the multi-span section is shown in Figure 13, along with the static pipeline configuration in the operational phase.

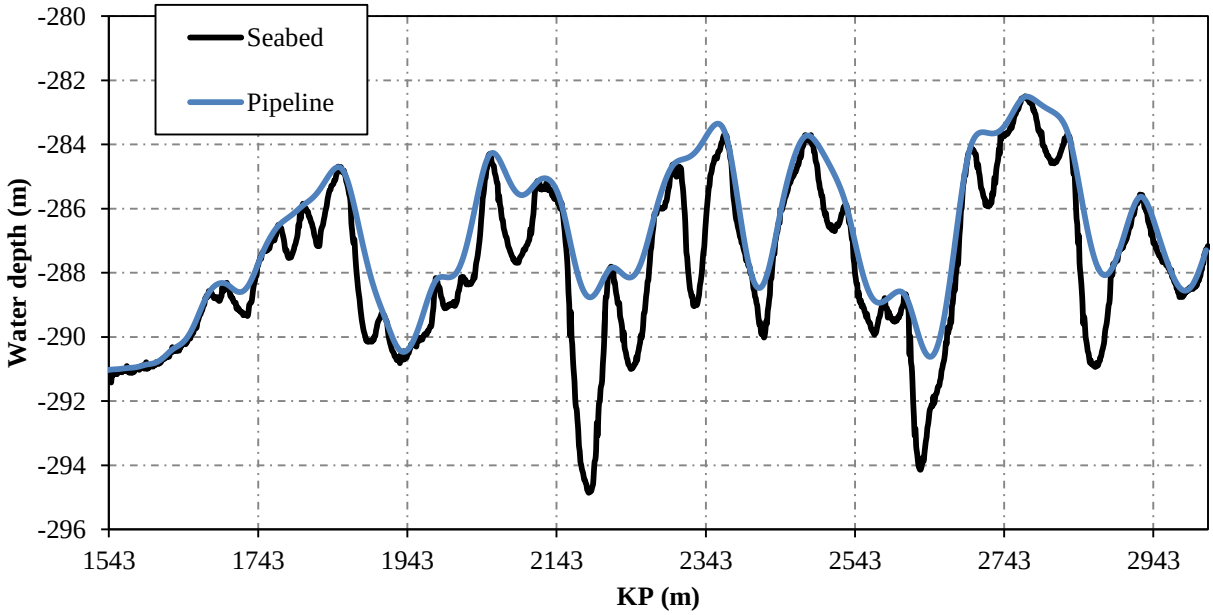


**Figure 13 – Seabed (black) and static pipeline configuration (blue) in operational condition as a function of KP for multi-span section 2.**

As was also the case for multi-span section 1, it is observed from the figure of multi-span section 2 that there is fairly uniform contact between pipe and seabed near each end of the section. Consequently, interaction with spans outside the multi-span section is not to be expected. Note that for the present case, it is a challenge to identify natural multi-span boundaries since the contact between the pipe and seabed is minimal along the entire length of the pipe. This explains why the chosen multi-span section is so long relative to the total length of the pipeline route. The pipeline geometry is given in Table 9.

**Table 9 – Pipe geometry.**

| Variable | Symbol | Unit | Value |
|---|---|---|---|
| Steel wall outer diameter | $D_s$ | mm | 254.3 |
| Steel wall thickness | $t_s$ | mm | 12.85 |
| 7-layer thermal insulation coating | $t_{coat}$ | mm | 50 |

Again, any variation in the effective axial force due to differences in thermal expansion coefficients and Poisson's ratios of the coating systems compared to the steel wall is disregarded. Relevant material properties and densities for the pipeline cross-section are given in Table 10.

**Table 10 – Material data.**

| Variable | Symbol | Unit | Value |
|---|---|---|---|
| Steel Young's modulus | $E$ | GPa | 201 |
| Thermal expansion coefficient of steel | $\alpha$ | $°C^{-1}$ | $1.05 \cdot 10^{-5}$ |
| Poisson's ratio of steel | $\nu$ | - | 0.3 |
| Density of steel | $\rho_{steel}$ | $kg/m^3$ | 7690 |
| Equivalent density of 7-layer coating | $\rho_{coat}$ | | 793 |
| Content density | $\rho_{cont}$ | | 150 |

Seabed properties for the route are presented in Table 11. The same seabed properties apply for the entire length of the pipeline.

**Table 11 – Seabed geotechnical properties.**

| Variable | Symbol | Unit | Value |
|---|---|---|---|
| Static vertical stiffness | $k_{v,s}$ | kN/m$^2$ | 300 |
| Axial friction coefficient | $\mu_{ax}$ | - | 0.2 |
| Lateral friction coefficient | $\mu_l$ | - | 0.2 |
| Dynamic vertical stiffness | $k_v$ | kN/m$^2$ | 5440 |
| Dynamic lateral stiffness | $k_l$ | | 3760 |
| Dynamic axial stiffness | $k_{ax}$ | | 3760 |

In both the static and dynamic analyses, PIPE31H elements with element lengths of 1 meter are used in Abaqus. Modal analyses are, of course, also performed with the SPFEA solver.

### 5.5 Multi-Span Section on Realistic Seabed – Case 3

A section of the seabed profile for the pipe corridor of a long gas export line is presented in Figure 14. The seabed has significant variations in water depth, which results in large rotations of the pipe elements in the static analysis. Thus, the example is suited to investigate the effects of including or excluding the added mass coefficient in the axial displacement direction, since the axial component of the modal response is expected to be large.

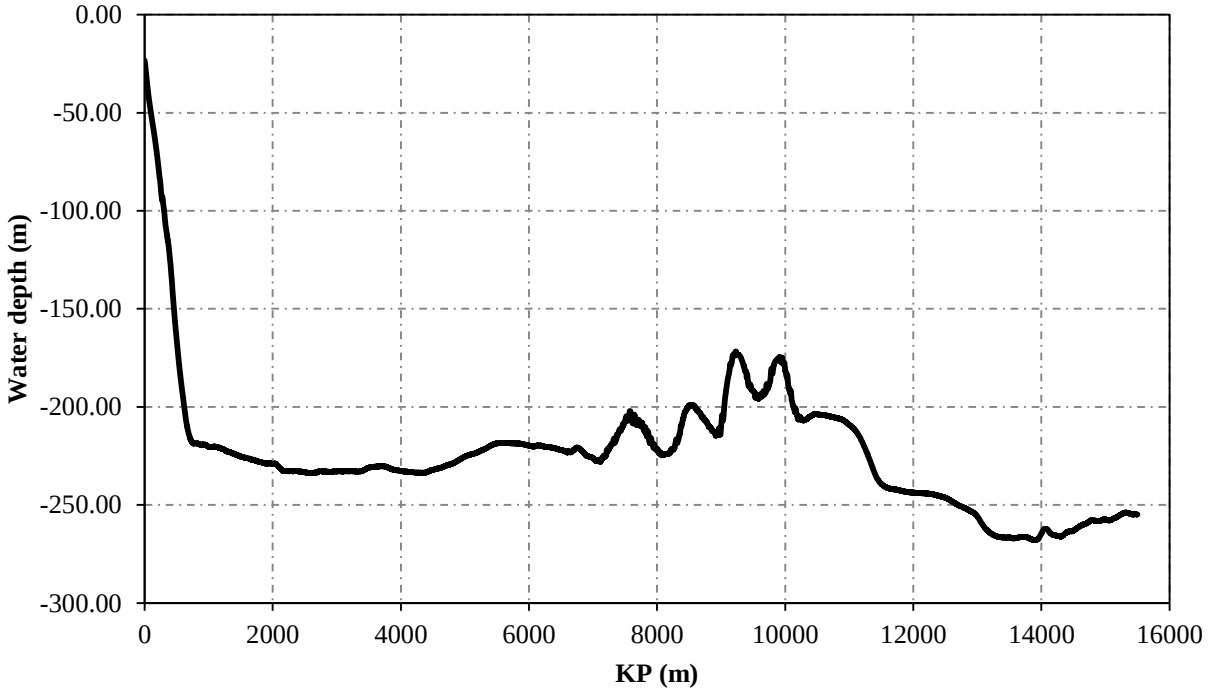


**Figure 14 – Seabed profile showing water depth as a function of kilometer point (KP).**

The region between KP 8162 and KP 9316 of the seabed profile shown in Figure 14 is selected as multi-span section 3. The multi-span section is presented in Figure 15, where the statically deformed pipeline is shown resting on the seabed in the operational phase.

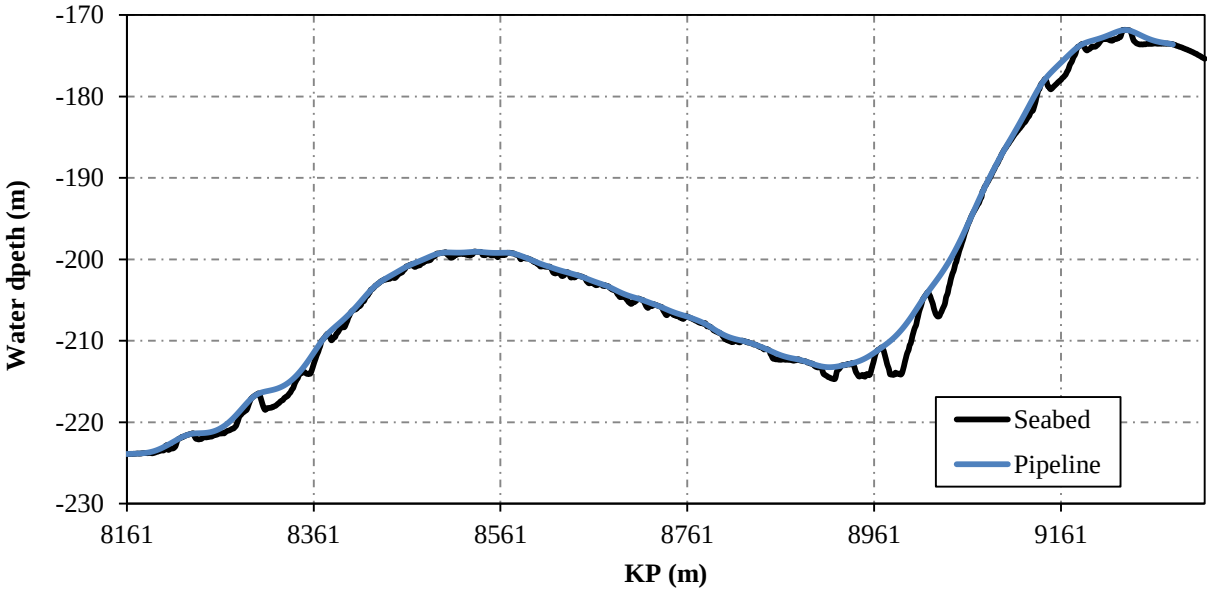


**Figure 15 – Seabed (black) and static pipeline configuration (blue) in operational condition as a function of KP for multi-span section 3.**

The water depth in the multi-span section varies between 172 and 223 meters. Several long spans are situated between KP 8961 and KP 9200, where the slope is approximately 14º. Hence, the rotations are significant in the spans, which should give rise to strong coupling between axial and transverse degrees of freedom.

The pipeline cross-sectional data are given in Table 12.

**Table 12 – Pipe geometry.**

| Variable | Symbol | Unit | Value |
|---|---|---|---|
| Steel wall outer diameter | $D_s$ | mm | 374.5 |
| Steel wall thickness | $t_s$ | mm | 29.5 |
| Asphalt enamel | $t_{coat,1}$ | mm | 6 |
| Concrete coating | $t_{coat,2}$ | mm | 55 |

Differences in material properties between the pipe steel and the coating layers may influence the effective axial force, but such effects are not accounted for. Material properties and densities are listed in Table 13.

**Table 13 – Material properties.**

| Variable | Symbol | Unit | Value |
|---|---|---|---|
| Steel Young's modulus | $E$ | GPa | 207 |
| Thermal expansion coefficient of steel | $\alpha$ | $°C^{-1}$ | $1.17 \cdot 10^{-5}$ |
| Poisson's ratio of steel | $\nu$ | - | 0.3 |
| Density of steel | $\rho_{steel}$ | $kg/m^3$ | 7850 |
| Density of asphalt coating | $\rho_{coat,1}$ | | 1300 |
| Density of concrete coating | $\rho_{coat,2}$ | | 3050 |
| Content density | $\rho_{cont}$ | | 0 |

Seabed properties for the route are presented in Table 14. The same seabed properties are applied for the entire pipeline section.

**Table 14 – Seabed geotechnical properties.**

| Variable | Symbol | Unit | Value |
|---|---|---|---|
| Static vertical stiffness | $k_{v,s}$ | $kN/m^2$ | 1500 |
| Axial friction coefficient | $\mu_{ax}$ | - | 0.45 |
| Lateral friction coefficient | $\mu_l$ | - | 0.45 |
| Dynamic vertical stiffness | $k_v$ | $kN/m^2$ | 11500 |
| Dynamic lateral stiffness | $k_l$ | | 7950 |
| Dynamic axial stiffness | $k_{ax}$ | | 7950 |

As in the two previous cases on realistic seabed profiles, PIPE31H elements with element lengths of 1 meter are used for the static Abaqus analyses. Modal analyses are carried out using the SPFEA solver only. However, the modal analyses are carried out both using an added mass coefficient of one and using an added mass coefficient of zero in the axial direction.

# 6 RESULTS AND DISCUSSIONS

## 6.1 Simply Supported Beam Model

A pipeline modeled as a simply supported beam, as described in Section 5.1, was investigated first. Below, in Figure 16, the lateral displacement configurations for the first four modes in-line, which were obtained using Abaqus (GPFEA) with B33 elements and by using the SPFEA solver, are shown.

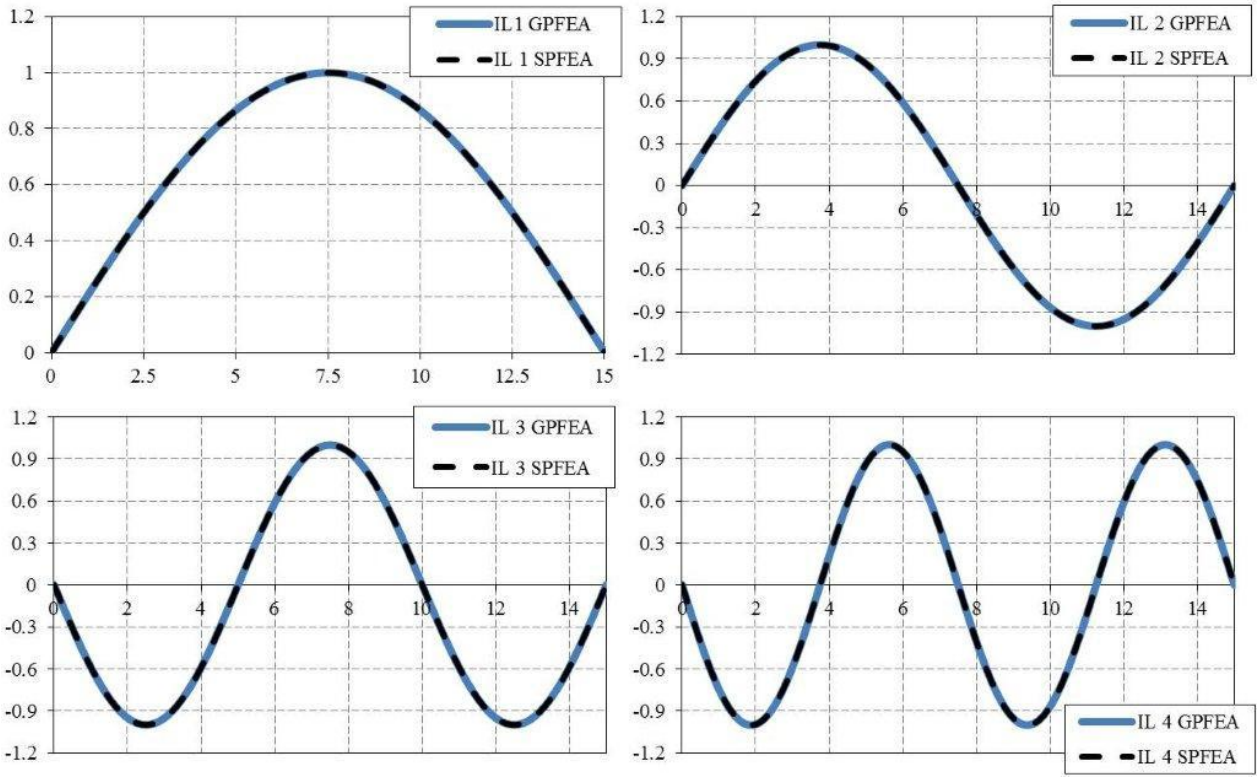


**Figure 16 – In-line mode shapes versus span length in meters for the first four modes obtained using Abaqus with B33 elements (GPFEA) and the SPFEA solver.**

From Figure 16 it is observed that the correspondence between the Abaqus and SPFEA solver is excellent with regard to mode shapes. In Table 15, the first 4 in-line frequencies are shown for the GPFEA, SPFEA and analytical solutions. From the results in Table 15, it is clear that the GPFEA solution with B33 elements gives near perfect correspondence to the analytical solution (Eq. (25)). The SPFEA solutions are marginally (in the fifth digit) higher than the

solutions from the B33 elements. The B33 element solution and the SPFEA solution differ in two minor ways:

1. The B33 elements are 3D beam elements, whereas the SPFEA elements are planar.
2. The eigenvalue solvers used are different. Abaqus uses the Lanczos algorithm [Hughes, 2000], while the SPFEA solution is based on the restarted Arnoldi iteration algorithm implemented in the "eigs" solver in Matlab [2010].

**Table 15 – Comparisons between the GPFEA and SPFEA in-line frequency results.**

| Mode number | GPFEA | | SPFEA | Analytical |
|---|---|---|---|---|
| | PIPE31H elements | B33 elements | | |
| 1 | 1.4370 | 1.4376 | 1.4378 | 1.4375 |
| 2 | 6.3597 | 6.3698 | 6.3704 | 6.3698 |
| 3 | 14.524 | 14.576 | 14.577 | 14.576 |
| 4 | 25.901 | 26.062 | 26.066 | 26.062 |

B33 elements are three-dimensional, which possibly makes the B33 elements marginally softer than the planar SPFEA elements. Indeed, small spurious vertical components were detected in the lateral in-line modes (not shown). Small deviations in the effective axial force distribution may also have a slight influence on the results. In both FE-solutions, the effective axial force varies slightly along the pipe length due to static deformation (between -44961 and -49999 N). The theoretical effective axial force, i.e., -45 kN according to Table 2, was used in the analytical solution, which may partly explain why the Euler-Bernoulli beam FE models behave slightly stiffer than the analytical solution.

From Table 15 it is also observed that the PIPE31H solution is marginally softer than the B33 (and SPFEA) element solutions. The difference between the solutions is explained by the differences in beam theories, i.e., that the PIPE31H elements are first order shear deformable Timoshenko beams, whereas the B33 elements are based on Euler-Bernoulli beam theory. It is expected that the introduction of shear deformation will lower the frequencies [Chopra, 2007; Shames and Dym, 1991], and it is demonstrated that the effect of shear deformation is marginal for all four modes in the present case.

Since the differences between the GPFEA solutions and the SPFEA results are negligible, and all the results have converged very well to the analytical solution, the SPFEA solution is considered verified for the pinned-pinned condition without any initial static deformation.

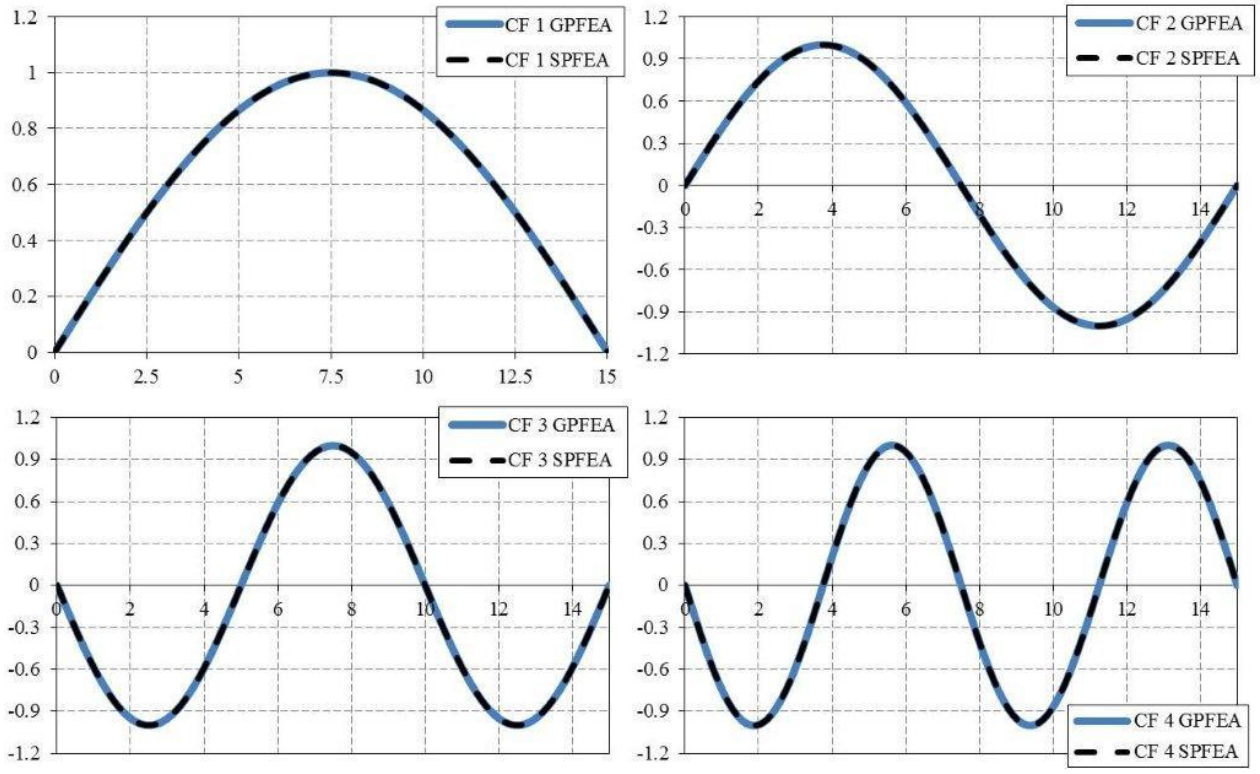


**Figure 17 – Cross-flow mode shapes versus span length in meters for the first four modes obtained using Abaqus with B33 elements (GPFEA) and the SPFEA solver.**

Vertical (cross-flow) mode shapes are plotted in Figure 17. As for the in-line case, it is observed that the correspondence between Abaqus and SPFEA is excellent. In Table 16, the first 4 cross-flow frequencies are listed for both the GPFEA and SPFEA solutions.

**Table 16 – Comparisons between the GPFEA and SPFEA cross-flow frequency results.**

| Mode number | GPFEA | | SPFEA |
|---|---|---|---|
| | PIPE31H elements | B33 elements | |
| 1 | 2.0093 | 2.0094 | 2.0094 |
| 2 | 6.3594 | 6.3694 | 6.3700 |
| 3 | 14.524 | 14.575 | 14.5769 |
| 4 | 25.9 | 26.062 | 26.0653 |

From Table 16, it is seen that the key observations made for the in-line frequency results still hold for the cross-flow case. The differences between the finite element solutions are marginal, and the effect of shear is negligible. Thus, for the statically deformed configuration, the SPFEA solution is also considered verified.

Moreover, it is readily observed that the fundamental cross-flow frequency is significantly higher than the corresponding in-line frequency. The differences between the cross-flow and in-line solutions, particularly for the fundamental mode, are explained by the static deformation caused by gravity. The rotation of the elements couples axial and bending stiffness, which causes a higher overall system stiffness, in turn giving rise to a higher natural frequency for the fundamental mode. A more detailed discussion on the effects of static deformation on free span dynamic response is given by Vedeld et al. [2013]. The curvature-dependence of the frequencies also explains why no simple analytical formula is available for this case.

### 6.2 Single Free Span on a Flat Seabed

The case of a single span on an idealized flat seabed, as described in Section 5.2, was studied next. The first four in-line mode shapes are shown in Figure 18.

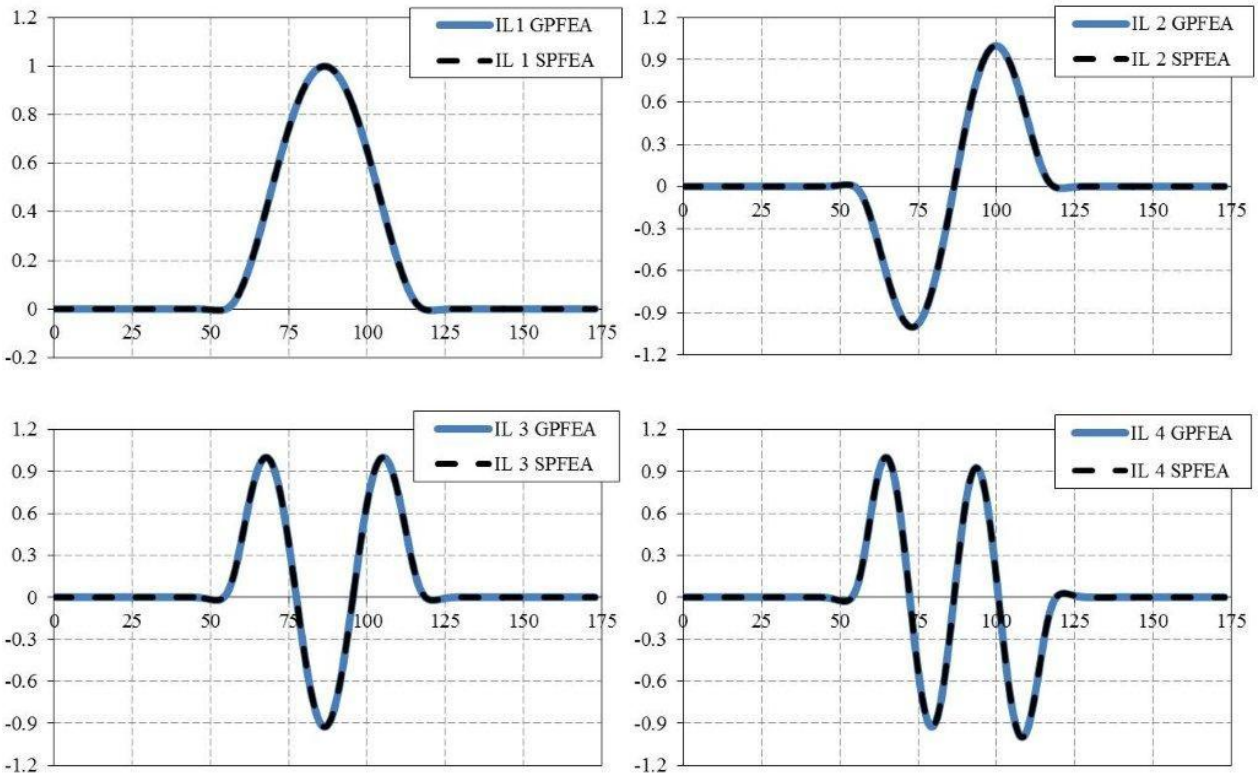


**Figure 18 – The first four in-line mode shapes calculated by Abaqus (GPFEA) and by SPFEA. The modes are plotted versus pipe length in meters.**

It is observed from the figure that there is perfect correspondence between the two FE solutions for the mode shapes. In Table 17 below, the frequencies corresponding to the first four in-line modes are given.

**Table 17 – Comparisons between the GPFEA and SPFEA in-line frequency results.**

| Mode number | GPFEA | | SPFEA |
|---|---|---|---|
| | PIPE31H elements | B33 elements | |
| 1 | 0.56138 | 0.5634 | 0.5634 |
| 2 | 1.548 | 1.5556 | 1.5557 |
| 3 | 3.0214 | 3.0423 | 3.0425 |
| 4 | 4.9559 | 5.0037 | 5.004 |

It is observed from Table 17 that the correspondence between the SPFEA results and B33 elements is excellent. The fundamental frequency calculated according to Eq. (26) is 0.560, which also is a very close match. Consequently, it may be concluded with confidence that both finite element solutions have been implemented correctly.

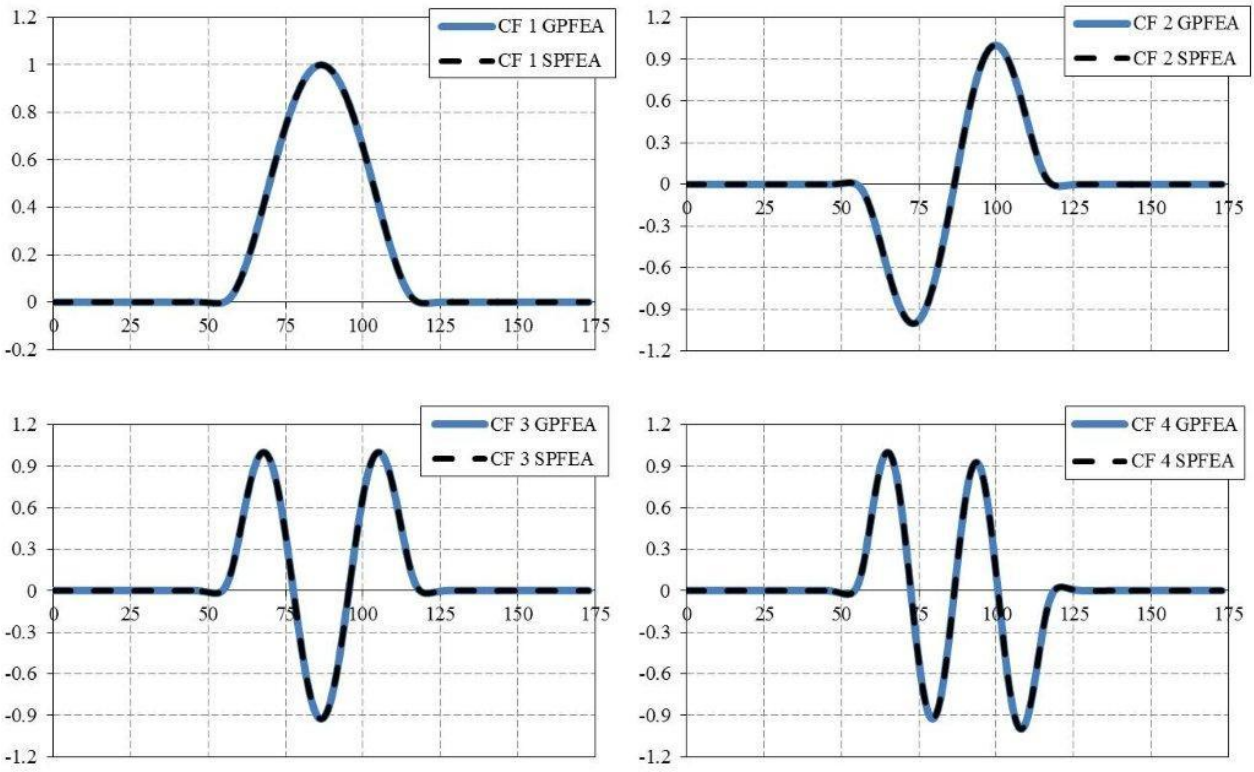


**Figure 19 – The first four cross-flow mode shapes calculated by Abaqus (GPFEA) and by SPFEA. The modes are plotted versus pipe length in meters.**

In Figure 19 above, the first four cross-flow mode shapes calculated by Abaqus and by SPFEA are displayed. From the figure it is observed, as in the previous cases, that the correspondence between the two FE solutions is excellent. The frequencies corresponding to the first cross-flow modes are presented below in Table 18.

**Table 18 – Comparisons between the GPFEA and SPFEA cross-flow frequency results.**

| Mode number | GPFEA | | SPFEA |
|---|---|---|---|
| | PIPE31H elements | B33 elements | |
| 1 | 0.58058 | 0.58225 | 0.5827 |
| 2 | 1.5693 | 1.5761 | 1.5776 |
| 3 | 3.0654 | 3.0864 | 3.0879 |
| 4 | 5.0325 | 5.082 | 5.0836 |

It is clear from Table 18 that the first four modes again match very closely in terms of frequencies. Using Eq. (26), the predicted fundamental frequency is 0.575, further demonstrating that the FE models have been implemented correctly.

### 6.3 Multi-Span Section on Realistic Seabed – Case 1

In Figure 20, the first four in-line mode shapes for multi-span section 1 (Section 5.3) are compared, with both the Abaqus and the SPFEA results presented. When examining multi-span sections, it is of interest to note whether neighboring spans interact. Span interaction may be inferred from the mode shapes by observing that there is a non-negligible modal response in several spans at the same time. Thus, while the fundamental mode for a single span typically has a symmetric mode shape of the type displayed in Figure 18 and Figure 19, the fundamental mode shape in a multi-span may be quite complex, consisting of a large peak in the main span and several smaller peaks in surrounding spans. On the rough seabed of multi-span section 1, interaction between neighboring spans is evident from all four mode shapes displayed in Figure 20, although the first two modes are dominated by the two longest spans in the area.

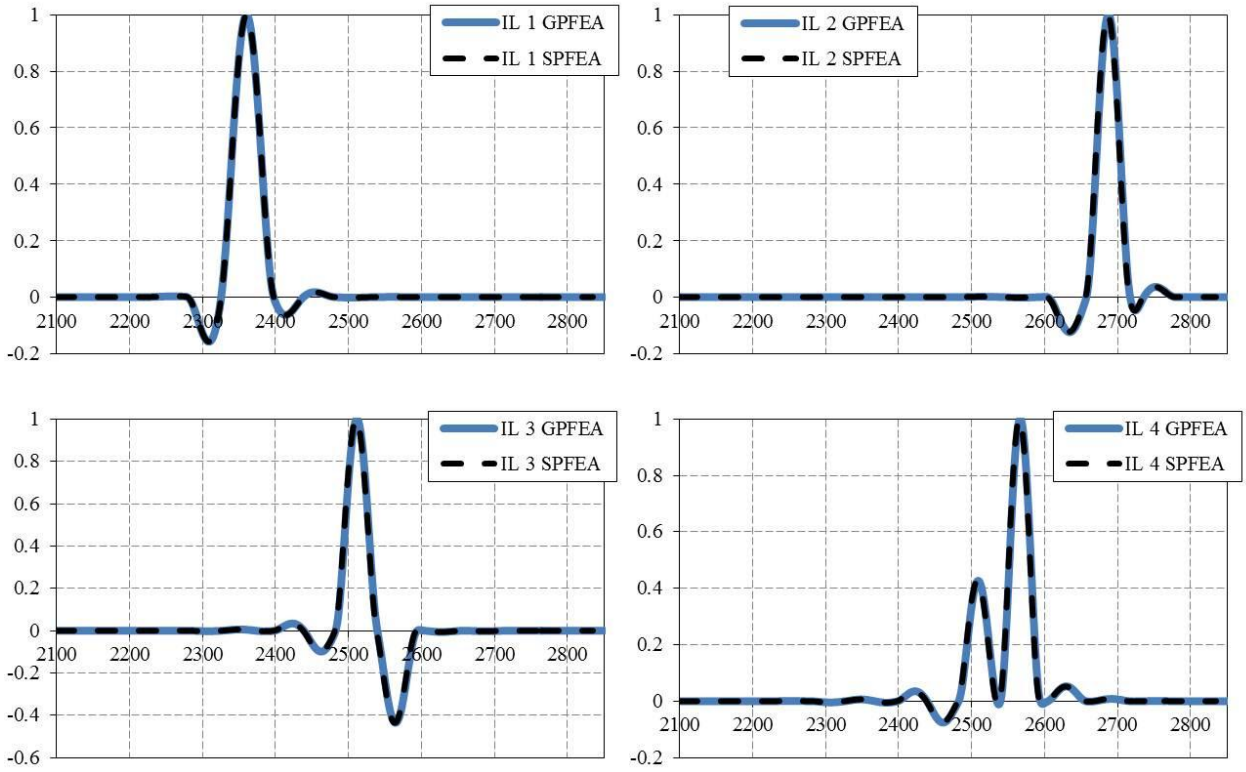


**Figure 20 - The first four in-line mode shapes calculated by Abaqus (GPFEA) and by the SPFEA solver. The mode shapes are plotted versus KP (in meters).**

It is further observed from the figure that the results from the two FE solutions are indistinguishable. In this case, the close correspondence between the FE models demonstrates that the SPFEA solver yields highly accurate results even for complex interacting modes.

In Figure 21, the first four cross-flow mode shapes from Abaqus and the SPFEA solver are compared. Modal interaction between spans is again evident from all four mode shapes, particularly for the third and fourth modes. It is further observed that the modal interaction is stronger in the cross-flow (Figure 21) than in the in-line (Figure 20) direction. Cross-flow modal interaction is partly dependent on rotation of the beam elements due to the undulating seabed. The rotation causes a coupling between vertical, rotational and axial degrees of freedom, which enhances modal interaction compared to the in-line response, where the axial and vertical displacements are completely decoupled. From Figure 21 it is also confirmed that the mode shapes calculated by the two FE solvers are indistinguishable.

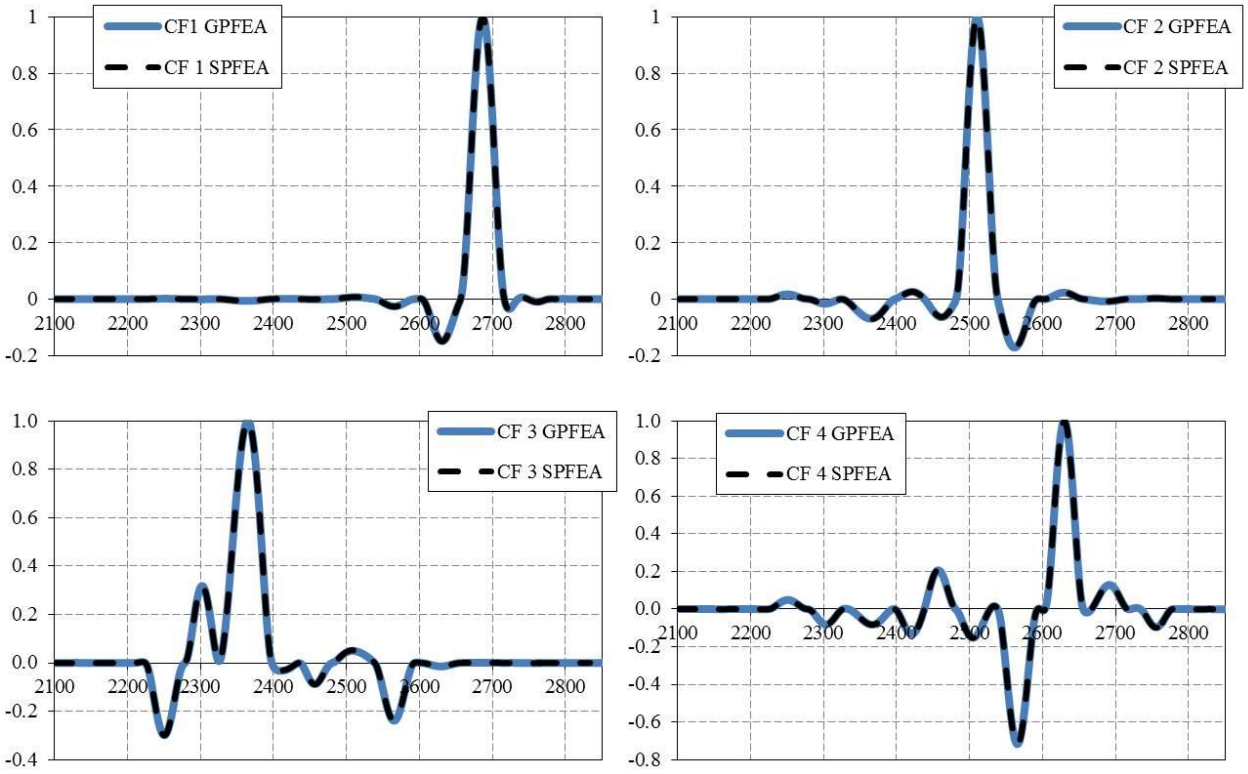


**Figure 21 - The first four cross-flow mode shapes calculated by Abaqus (GPFEA) and by the SPFEA solver. The mode shapes are plotted versus KP (in meters).**

**Table 19 – The first 15 in-line and cross-flow modal frequencies.**

| Mode number | In-line | | | Cross-flow | | |
|---|---|---|---|---|---|---|
| | GPFEA | SPFEA | Ratio | GPFEA | SPFEA | Ratio |
| 1 | 0.20081 | 0.20091 | 0.99948 | 0.34454 | 0.34424 | 1.00088 |
| 2 | 0.32462 | 0.32417 | 1.00139 | 0.38052 | 0.38050 | 1.00005 |
| 3 | 0.35553 | 0.35554 | 0.99996 | 0.40757 | 0.40737 | 1.00050 |
| 4 | 0.42688 | 0.42674 | 1.00033 | 0.51499 | 0.51524 | 0.99952 |
| 5 | 0.45594 | 0.45619 | 0.99944 | 0.54941 | 0.54949 | 0.99986 |
| 6 | 0.46302 | 0.46407 | 0.99773 | 0.56691 | 0.56746 | 0.99904 |
| 7 | 0.50584 | 0.50644 | 0.99882 | 0.60749 | 0.60791 | 0.99931 |
| 8 | 0.52901 | 0.52932 | 0.99941 | 0.67551 | 0.67590 | 0.99943 |
| 9 | 0.62495 | 0.62430 | 1.00104 | 0.68889 | 0.69030 | 0.99796 |
| 10 | 0.66094 | 0.66163 | 0.99896 | 0.76631 | 0.76674 | 0.99944 |
| 11 | 0.75449 | 0.75501 | 0.99931 | 0.83981 | 0.83996 | 0.99982 |
| 12 | 0.95637 | 0.95649 | 0.99987 | 0.98956 | 0.98985 | 0.99971 |
| 13 | 1.05250 | 1.05321 | 0.99932 | 1.10230 | 1.10324 | 0.99915 |
| 14 | 1.07600 | 1.07632 | 0.99971 | 1.12390 | 1.12441 | 0.99954 |
| 15 | 1.22440 | 1.22547 | 0.99913 | 1.25690 | 1.25779 | 0.99929 |

Eigenfrequencies associated with the first 15 in-line and cross-flow modes of multi-span section 1 are listed in Table 19. It is seen from the table that the GPFEA- and SPFEA-derived frequencies match substantially. In fact the largest relative difference is 0.2% for mode 9 cross-flow, and most other relative differences are less than 0.1%. Given that the mode shapes also match excellently, the SPFEA model is considered verified for the present case. Note also that shear-flexible PIPE31H elements were applied in the GPFEA. Consequently, it has been clearly demonstrated that the effect of disregarding shear deformation is negligible.

### 6.4 Multi-Span Section on Realistic Seabed – Case 2

The results for multi-span section 2 on realistic seabed are similar to the results from multi-span section 1 (Section 6.3). However, in multi-span section 2 there is less contact between the pipe and the seabed, making the modal analyses particularly challenging.

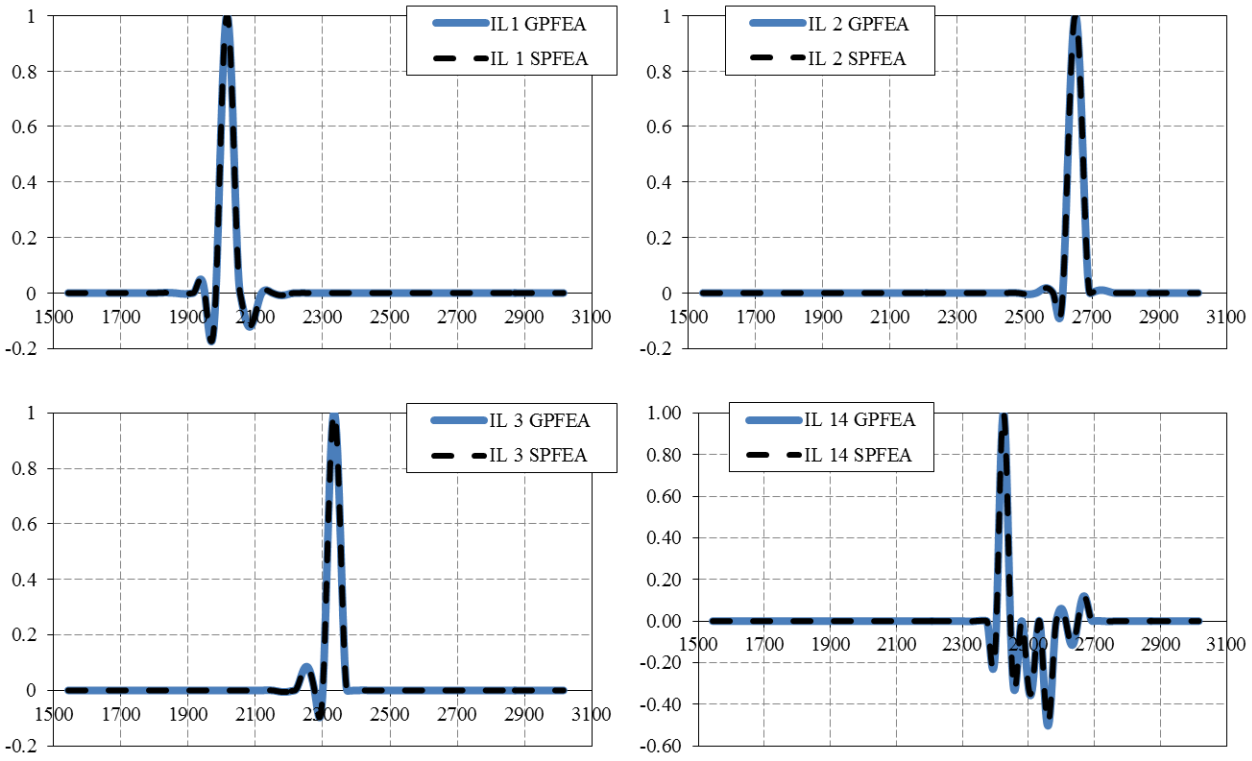


**Figure 22 - The first three in-line mode shapes calculated by Abaqus (GPFEA) and by the SPFEA solver. In addition mode number 14 is shown to illustrate span interaction. The mode shapes are plotted versus KP (in meters).**

In Figure 22, the mode shapes for the first three in-line modes, as well as the fourteenth in-line mode, are shown for the Abaqus and SPFEA solutions. Mode 14 was included in the comparison to demonstrate the correspondence between the two solutions even for highly complex mode shapes. As observed in the previous comparisons, the solutions for the two FE solvers are indistinguishable.

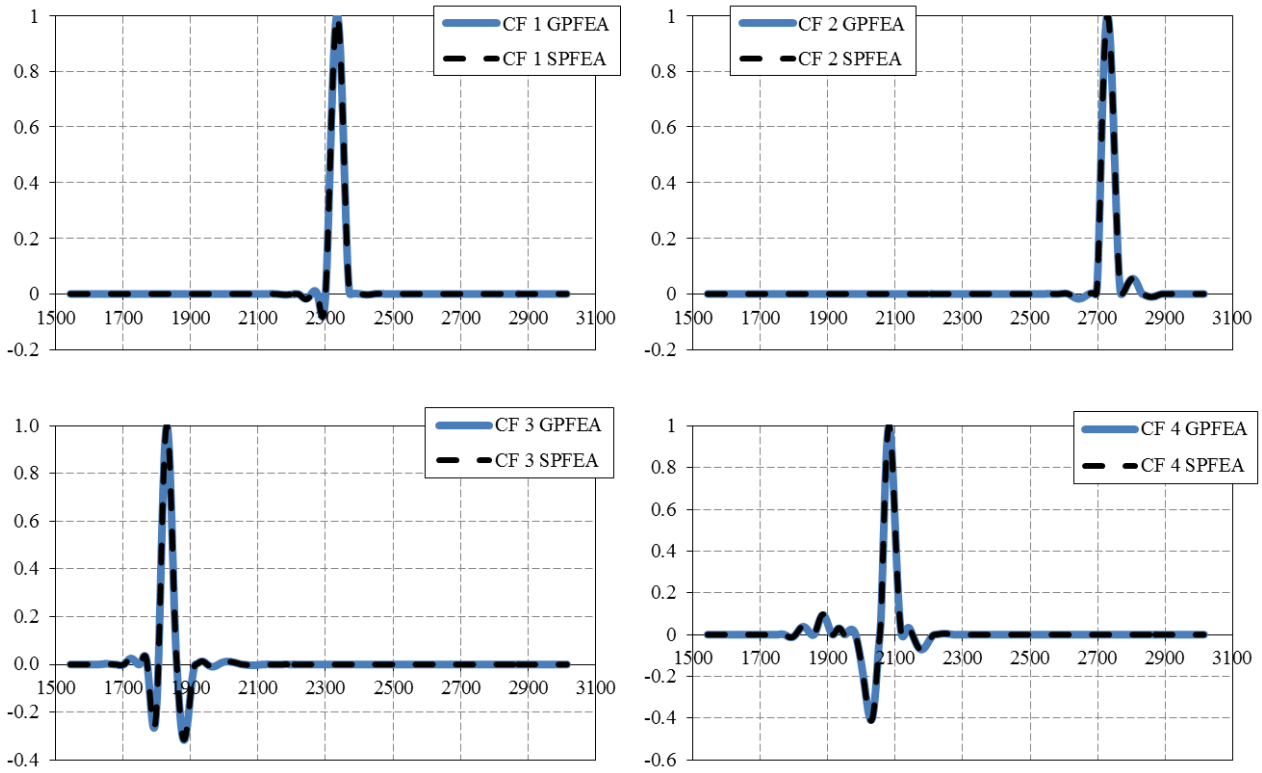


**Figure 23 - The first four cross-flow mode shapes calculated by Abaqus (GPFEA) and by the SPFEA solver. The mode shapes are plotted versus KP (in meters).**

The mode shapes produced by the two FE solvers match perfectly also for the first four cross-flow modes, as shown in Figure 23. In Table 20 the eigenfrequencies corresponding to the first 15 in-line and cross-flow modes are presented for both the Abaqus and the SPFEA solutions. The strong agreement between the two FE solutions applies also for the frequencies. The largest relative deviation between corresponding values of in-line frequency is approximately 1%, and the largest deviation cross-flow is about 0.7%.

**Table 20 - The first 15 in-line and cross-flow modal frequencies.**

| Mode number | In-line | | | Cross-flow | | |
|---|---|---|---|---|---|---|
| | GPFEA | SPFEA | Ratio | GPFEA | SPFEA | Ratio |
| 1 | 0.10363 | 0.10324 | 1.00374 | 0.12888 | 0.12982 | 0.99277 |
| 2 | 0.10788 | 0.10787 | 1.00009 | 0.17001 | 0.17033 | 0.99811 |
| 3 | 0.12578 | 0.12702 | 0.99027 | 0.18186 | 0.18193 | 0.99964 |
| 4 | 0.15352 | 0.15498 | 0.99057 | 0.24227 | 0.24291 | 0.99736 |
| 5 | 0.15438 | 0.15429 | 1.00059 | 0.24398 | 0.24406 | 0.99967 |
| 6 | 0.16311 | 0.16303 | 1.00050 | 0.25774 | 0.25825 | 0.99804 |
| 7 | 0.16474 | 0.16528 | 0.99673 | 0.27113 | 0.27043 | 1.00261 |
| 8 | 0.20854 | 0.20889 | 0.99831 | 0.32653 | 0.32525 | 1.00394 |
| 9 | 0.20917 | 0.20944 | 0.99869 | 0.34017 | 0.33959 | 1.00172 |
| 10 | 0.21386 | 0.21442 | 0.99741 | 0.39572 | 0.39636 | 0.99839 |
| 11 | 0.234 | 0.23435 | 0.99849 | 0.42858 | 0.42918 | 0.99861 |
| 12 | 0.23481 | 0.23533 | 0.99779 | 0.42933 | 0.42862 | 1.00166 |
| 13 | 0.2934 | 0.29392 | 0.99822 | 0.48061 | 0.48152 | 0.99812 |
| 14 | 0.30907 | 0.30961 | 0.99824 | 0.49038 | 0.49053 | 0.99970 |
| 15 | 0.32447 | 0.32480 | 0.99899 | 0.49419 | 0.49383 | 1.00074 |

Based on the data presented in the current and the preceding sections, it may be concluded that the SPFEA solver has been correctly implemented and can be considered verified. Furthermore, since shear-deformable PIPE31H elements were applied in the Abaqus analyses also for multi-span section 2, it has been shown that Euler-Bernoulli beam theory is sufficient for accurate prediction of pipeline modal response, in agreement with previous findings [Fyrileiv and Mørk, 2002; Vedeld et al., 2013].

### 6.5 Effects of Consistent Soil Stiffness Formulation

As described in Section 3, two different ways of modeling the soil stiffness have been implemented in the SPFEA solver. Conventionally, the soil is modeled using discrete springs in the axial, lateral and vertical directions, as illustrated in Figure 9. Thus, the stiffness of the soil is idealized as lumped or concentrated at the pipe nodes, and the soil provides no direct rotational stiffness. Usually, the lumped soil stiffness approach is satisfactory, and the lumped approach will also converge toward a consistent soil stiffness formulation (as given by Eq. (19)) when increasing the number of elements. However, for very rough seabed configurations with short intermediate shoulders in-between spans, the effect of disregarding rotational stiffness, as well as the stiffness coupling between translational and rotational degrees of freedom, may be non-

negligible even for very short element lengths. These effects will be studied in some detail in the present section.

As described previously, the element length was set to 1 m for both cases with pipelines resting on realistic seabed (i.e., multi-span sections 1 and 2), which corresponded to the resolution of the seabed survey data. Thus, in the lumped formulation discrete springs were placed at the nodes, each with a stiffness corresponding to 0.5 m pipe-soil contact on each side of the node. In the consistent formulation, on the other hand, the soil is modeled as continuous over the element length, with a stiffness corresponding to the average of the two nodal stiffness values, as seen from Eq. (20). Hence, at the end of each shoulder, the soil stiffness is reduced by a factor of two. However, the pipe-soil contact will be extended by half an element's length relative to the lumped formulation (where the shoulder as mentioned ends halfway between nodes). Consequently, although the integrated translational stiffness contribution from the soil should be the same in the two formulations, each span will be shortened by in total one element length (i.e., a half element length on each shoulder) when applying the consistent soil formulation with the same element resolution.

From Eqs. (25) and (26) it is evident that the modal frequencies decrease rapidly with the span length. Since span lengths are based on the bottom roughness analysis, we will assume in the following that the lumped formulation gives correct span lengths. With the consistent soil stiffness approach, the span shoulders are consequently slightly too long, and the associated frequencies may therefore be overestimated. To summarize, the lumped formulation will likely underestimate modal frequencies due to the lack of rotational stiffness, whereas the consistent formulation will likely overestimate modal frequencies since span lengths are marginally too long. Both effects are likely to be most influential when the shoulders are very short. It should, however, be noted that the inaccuracies will tend to zero for increasing element refinement.

In Table 21, in-line and cross-flow frequencies are shown for both the consistent and lumped soil stiffness models for multi-span section 1, which was described in Section 5.3. From the table, it is observed that the relative differences between the frequencies for the two soil modeling approaches are generally in the range of 1% to 3.5%. Thus, the effect of span length and rotational stiffness of the soil, as described above, does not have a particularly large impact on the frequencies of the modal response in multi-span section 1. The effects on the mode shapes are, as we will see, more notable in a few cases.

**Table 21 – The first 15 in-line and cross-flow frequencies for the lumped and consistent soil models in multi-span section 1 (described in Section 5.3).**

| Mode number | In-line | | | Cross-flow | | |
|---|---|---|---|---|---|---|
| | Lumped soil stiffness | Consistent soil stiffness | Ratio | Lumped soil stiffness | Consistent soil stiffness | Ratio |
| 1 | 0.20091 | 0.206325 | 0.973772 | 0.34424 | 0.350253 | 0.982828 |
| 2 | 0.32417 | 0.329761 | 0.983043 | 0.38050 | 0.38746 | 0.982045 |
| 3 | 0.35554 | 0.363335 | 0.978556 | 0.40737 | 0.410472 | 0.992436 |
| 4 | 0.42674 | 0.431452 | 0.989079 | 0.51524 | 0.521394 | 0.988195 |
| 5 | 0.45619 | 0.462109 | 0.987202 | 0.54949 | 0.568764 | 0.966105 |
| 6 | 0.46407 | 0.469948 | 0.987502 | 0.56746 | 0.578126 | 0.981544 |
| 7 | 0.50644 | 0.521351 | 0.971392 | 0.60791 | 0.615355 | 0.987901 |
| 8 | 0.52932 | 0.544786 | 0.971618 | 0.67590 | 0.683956 | 0.988216 |
| 9 | 0.62430 | 0.635133 | 0.982941 | 0.69030 | 0.700414 | 0.985555 |
| 10 | 0.66163 | 0.66807 | 0.990361 | 0.76674 | 0.776087 | 0.987951 |
| 11 | 0.75501 | 0.762015 | 0.990813 | 0.83996 | 0.847181 | 0.991474 |
| 12 | 0.95649 | 0.968174 | 0.987935 | 0.98985 | 1.00292 | 0.986964 |
| 13 | 1.05321 | 1.067263 | 0.986837 | 1.10324 | 1.118988 | 0.985928 |
| 14 | 1.07632 | 1.092755 | 0.984957 | 1.12441 | 1.144134 | 0.982765 |
| 15 | 1.22547 | 1.236083 | 0.99141 | 1.25779 | 1.270525 | 0.98998 |

Generally, when introducing rotational soil stiffness as well as slightly increasing the lengths of the span shoulders, one would expect the interaction between neighboring spans to be reduced. A pattern with slightly smaller side-span amplitudes for the consistent soil formulation was also observed from the data. In-line modes 1 and 3 are shown in Figure 24 for the two soil models. As observed from the figure, the influence of soil modeling is hardly detectable for the in-line response modes, with side span amplitudes only marginally lower for the consistent soil stiffness model.

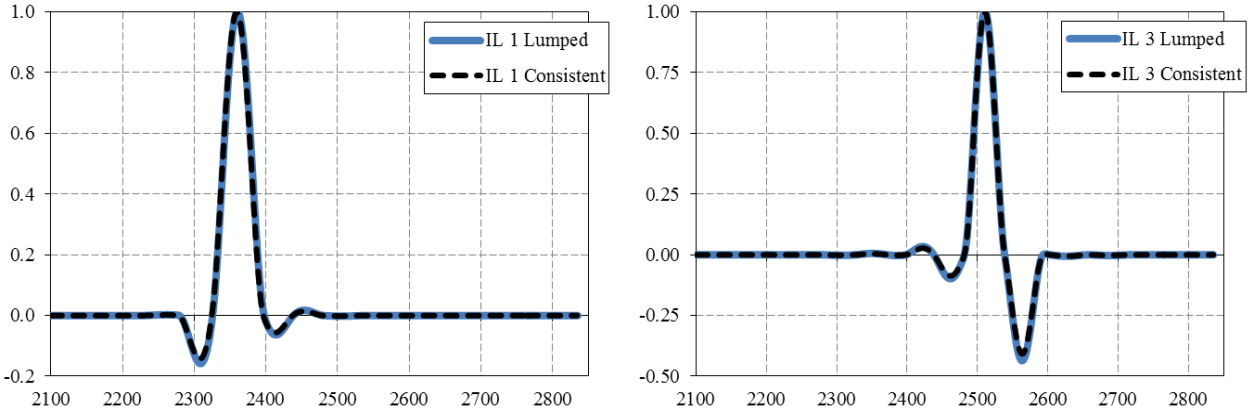


**Figure 24 – In-line modal response in multi-span section 1 (described in Section 5.3) for modes 1 and 3 using lumped and consistent soil stiffness formulations.**

Representative cross-flow modal responses are shown in Figure 25. It is observed from the figure that mode 4 is relatively uninfluenced by the change in soil stiffness formulation (only marginally lower side-span amplitudes), whereas mode 5 surprisingly displays higher degree of span interaction for the consistent mass formulation. Hence, it is demonstrated that the choice of stiffness model may have a non-negligible influence on the mode shapes in interacting spans. Mode 5 is presented because the difference in mode shapes is somewhat significant. However, typical influence from the soil model on the mode shape is best illustrated by the comparison between the mode shapes corresponding to mode 4, i.e., for multi-span section 1, the difference between mode shapes was generally seen to be quite small, with side span amplitudes slightly lower when the consistent mass formulation was applied (in contrast to the observation for mode shape 5, where side span amplitudes are higher for the consistent mass formulation).

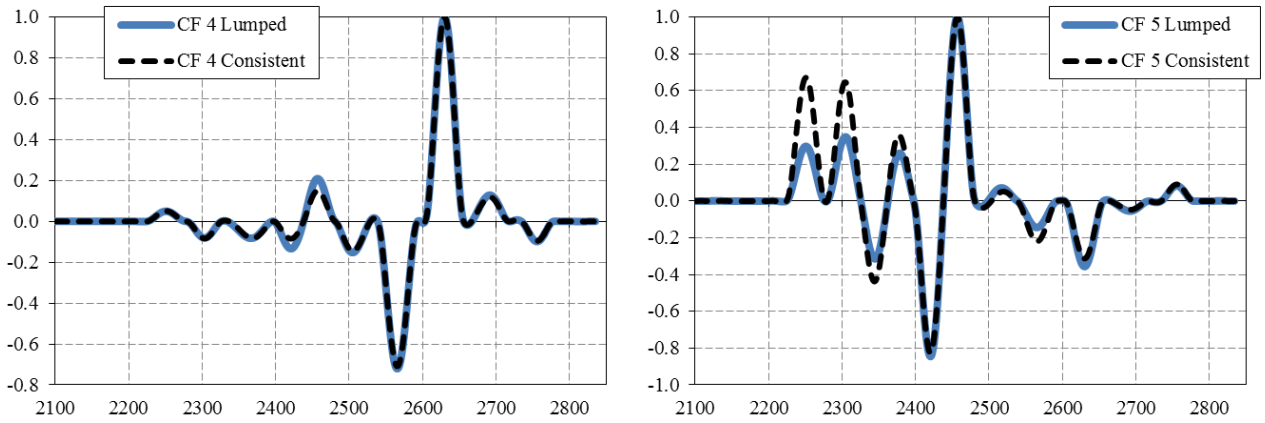


**Figure 25 – Cross-flow modal response in multi-span section 1 (described in Section 5.3) for modes 4 and 5 using lumped and consistent soil stiffness formulations.**

As remarked above, there is a coupling between the axial and vertical degrees of freedom when the static displacements and rotations due to gravity and seabed topography are introduced. The introduction of rotational soil stiffness and additional coupling between translational and rotational degrees of freedom may in part explain why span interaction for a few cross-flow modes appeared to be enhanced when applying the consistent soil model.

The same comparisons between results for lumped and consistent soil formulations as were made for multi-span section 1 (Section 5.3) are also made for multi-span section 2 (Section 5.4). In-line and cross-flow modal frequencies are compared in Table 22. Note that for both the in-line and the cross-flow direction, the fourteenth mode obtained with the lumped formulation did not have a matching mode among the fifteen modes calculated using the consistent formulation.

**Table 22 - The first 15 in-line and cross-flow frequencies for the lumped and consistent soil models in multi-span section 2 (described in Section 5.4).**

| Mode number | In-line | | | Cross-flow | | |
|---|---|---|---|---|---|---|
| | Lumped soil stiffness | Consistent soil stiffness | Ratio | Lumped soil stiffness | Consistent soil stiffness | Ratio |
| 1 | 0.10324 | 0.11850 | 0.87125 | 0.12982 | 0.13942 | 0.93115 |
| 2 | 0.10787 | 0.11463 | 0.94104 | 0.17033 | 0.17460 | 0.97558 |
| 3 | 0.12702 | 0.13590 | 0.93460 | 0.18193 | 0.22129 | 0.82211 |
| 4 | 0.15429 | 0.16813 | 0.91768 | 0.24291 | 0.25541 | 0.95108 |
| 5 | 0.15498 | 0.15765 | 0.98307 | 0.24406 | 0.24847 | 0.98224 |
| 6 | 0.16303 | 0.17221 | 0.94669 | 0.25825 | 0.27060 | 0.95435 |
| 7 | 0.16528 | 0.20144 | 0.82051 | 0.27043 | 0.28804 | 0.93886 |
| 8 | 0.20889 | 0.23903 | 0.87393 | 0.32525 | 0.34296 | 0.94835 |
| 9 | 0.20944 | 0.22466 | 0.93226 | 0.33959 | 0.35341 | 0.96088 |
| 10 | 0.21442 | 0.22174 | 0.96696 | 0.39636 | 0.43912 | 0.90262 |
| 11 | 0.23435 | 0.23825 | 0.98366 | 0.42862 | 0.45423 | 0.94362 |
| 12 | 0.23533 | 0.24662 | 0.95421 | 0.42918 | 0.44263 | 0.96961 |
| 13 | 0.29392 | 0.31320 | 0.93845 | 0.48152 | 0.51075 | 0.94277 |
| 14 | 0.30961 | - | - | 0.49053 | - | - |
| 15 | 0.32480 | 0.33868 | 0.95900 | 0.49383 | 0.51891 | 0.95166 |

From Table 22 it is observed that the differences between the results for the two soil modeling approaches are much more pronounced than for multi-span section 1. In fact, the maximum differences in modal frequencies are as high as ~18% both the in-line (mode 7) and the cross-flow (mode 3) direction. It can also be seen from the table that the sequence of modes to some extent changes depending on the soil modeling, for instance the first in-line mode with lumped soil corresponds to the second mode with a consistent soil. The large influence of the chosen soil model is easily explained when inspecting the results in more detail. In Figure 26, in-line modes 1 (Figure 26 a) and 4 (Figure 26 b) are displayed. Note that the mode numbers refer to the lumped soil results. The corresponding mode numbers are 2 and 5 with the consistent soil model. In order to highlight the causes of the large differences between the soil modeling approaches, the relevant section of the static pipe configuration is also shown (Figure 26 c).

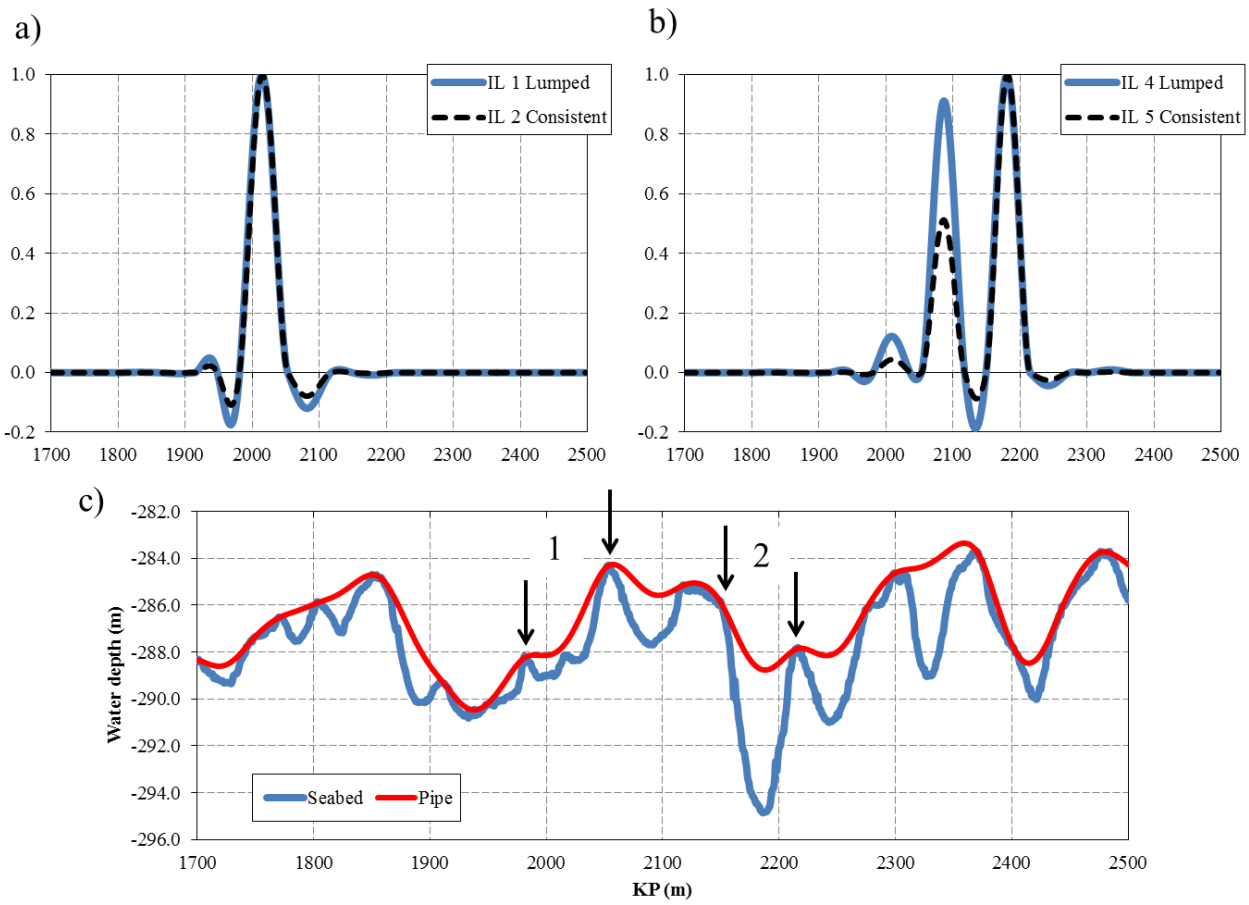


**Figure 26 – In-line modal response in multi-span section 2 (described in Section 5.4) for mode 1 (a) and mode 4 (b) using lumped and consistent soil stiffness models. A section of the static pipe configuration is also shown (c), with the dominant spans from in-line mode 1 (span 1) and mode 4 (span 2) indicated.**

Multi-span section 2 is characterized by a highly undulated seabed, with a stiff clayey soil. In addition, the pipeline has a very small specific weight. The combination of these factors results in very sporadic pipe-soil contact, implying that the intermediate span shoulders are few and short. The presence of a large number of spans is easily observed from Figure 26 c). All the spans between KP 1900 and KP 2300, corresponding to the middle of the section exhibited in Figure 26 c), are listed in Table 23 below.

The 70-m long span denoted “1” in Figure 26 c) corresponds to the dominating span of the first in-line mode (Figure 26 a). Despite the very short touchdown-areas on either side of the dominating span, the influence on the mode shape of introducing a consistent soil model is modest. However, a significant stiffening effect is seen from the modal frequency, which is

increased by almost 15% when applying consistent soil modeling. A more pronounced impact on the mode shape is observed for mode 4 (Figure 26 b), where the amplitudes in spans 1, *iii* and *iv* (see Table 23) are significantly reduced for the consistent soil model approach.

**Table 23 – List of spans between KP 1900 and KP 2300 of multi-span section 2.**

| Span number | Left touchdown point (KP) | Right touchdown point (KP) | Span length (m) |
|---|---|---|---|
| *i* | 1916 | 1949 | 32 |
| *ii* | 1949 | 1982 | 32 |
| 1 | 1982 | 2053 | 70 |
| *iii* | 2055 | 2118 | 62 |
| *iv* | 2119 | 2150 | 30 |
| 2 | 2151 | 2215 | 63 |
| *v* | 2218 | 2275 | 56 |
| *vi* | 2276 | 2300 | 23 |

It may further be observed from Table 23 that the number of nodes (one node per KP) with pipe-soil contact in-between the spans often is in the range from 1 to 3. As mentioned previously, the difference between the soil modeling approaches is expected to be most pronounced for very short intermediate span shoulders, which is exactly what we have demonstrated by comparing the results of multi-span section 1 and multi-span section 2. It is also physically obvious that the introduction of rotational stiffness will have a large impact when there is a single contact node in the lumped formulation. For this reason, DNV-RP-F105 recommends to ensure contact between at least two nodes at each span shoulder in order to obtain realistic rotational pipe-soil stiffness [DNV-RP-F105, 2006].

The largest deviation in cross-flow frequencies between the two soil modeling approaches was observed for mode 3, for which the lumped soil model frequency was almost 18% lower than the corresponding frequency for consistent soil. The associated mode shapes are shown in Figure 27. Despite the significant difference in modal frequencies, it is observed that the mode shapes fit into the general pattern of moderate reduction in side-span amplitudes for the consistent soil formulation. This is also seen for mode shape 4, which is plotted to the right in the figure. However, for a few of the higher mode numbers, the same increase in side-span amplitudes as demonstrated for cross-flow mode 5 in multi-span section 1 (Figure 25) when applying consistent pipe-soil stiffness, was observed again for multi-span section 2 (not shown).

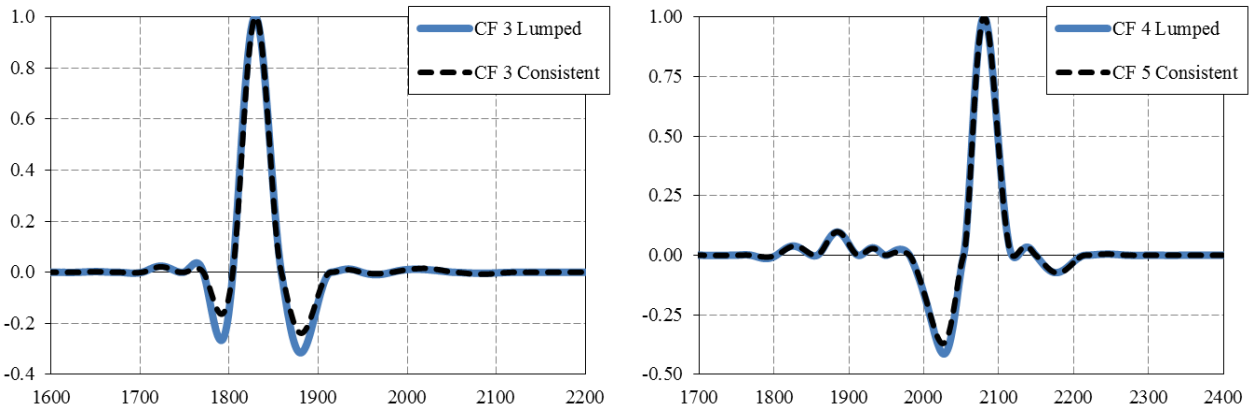


**Figure 27 – Cross-flow modal response in multi-span section 2 (described in Section 5.4) for mode 3 (a) and mode 4 (b) using lumped and consistent soil stiffness models.**

### 6.6 Effect of Axial Added Mass Formulation

A modal analysis of multi-span section 3 was conducted using a consistent soil stiffness formulation. The modal analysis was performed twice; once with an added mass coefficient of one in axial direction, and then repeated with an added mass coefficient of zero in axial direction. The resulting modal responses were negligibly influenced by the added mass in axial direction, where the changes in the first 15 modal frequencies were only about 0.00 – 0.20%.

Hence, even for a case where the rotations are significant, in the range of 14º, there is negligible influence on the modal response from applying zero added mass in axial direction, despite the significant coupling between axial and vertical degrees of freedom in this particular pipeline scenario.

### 6.7 On the Use of SPFEA versus GPFEA

In the preceding sections 6.1-6.4, results of modal analyses carried out with the SPFEA solver were compared to results of GPFEA with the commercially available software Abaqus [2012]. The correspondence was demonstrated to be excellent, with less than one percent deviation even for higher order eigenfrequencies of pipelines in interacting multi-spans. Similarly, the mode shapes obtained by SPFEA and GPFEA were found to be indistinguishable. Hence, it has been demonstrated that the SPFEA solver developed and presented in the present

report may be applied for modal analysis of multi-span pipelines without loss of accuracy compared to GPFEA with shear-deformable pipe elements.

The extensive comparisons between SPFEA and GPFEA have provided insights into advantages and drawbacks related to the two analysis methodologies. With regard to physical modeling of multi-span pipelines, there are two distinct advantages associated with SPFEA; namely the possibility of applying a consistent soil modeling and of applying separate added mass coefficients in the axial and transverse directions. While the former effect was shown to be significant in cases with very short intermediate span shoulders (Section 6.5), the latter was seen to be completely negligible (Section 6.6). An advantage of using GPFEA, on the other hand, is the availability of 3D pipe elements based on Timoshenko beam theory. However, the comparisons to SPFEA results convincingly demonstrate that the loss of accuracy introduced by applying planar Euler-Bernoulli beam elements is negligible for modal analyses of multi-span offshore pipelines. It should also be noted that the first order PIPE31H element in Abaqus does not apply a consistent mass matrix, but a lumped mass matrix formulation, in which the coupling terms between the transverse and rotational degrees of freedom are disregarded.

For PIPE31H elements, and generally for beam circular cross-sections, Abaqus calculates the second moment of area $I$ based on a thin-wall formulation, i.e., $I = \pi R^3 t$, where $R$ is the mean pipe-wall radius and $t$ is the wall thickness. The exact expression is $I = \pi(D_s^4 - D_i^4)/64$, , where $D_s$ is the outer diameter and $D_i$ the inner diameter of the pipe steel. The expressions may deviate by a few percent for thick-walled pipes. Obviously, the exact expression may be adopted in the SPFEA solver, although the thin-wall formulation - for best correspondence to Abaqus results - was used in the analyses presented in this report.

The most significant advantages of applying the SPFEA solver rather than GPFEA are of practical nature. The modal analysis procedure in Abaqus was outlined in Section 4.2. As noted there, new element sets, node sets and contact pairs must be defined for each multi-span section, each of which is identified based on the results of the bottom roughness analysis. However, the static analysis must be redone prior to the modal analysis because new contact pairs and node sets cannot be introduced when restarting the analysis in a load step corresponding to the relevant pipeline condition (i.e., as-laid, water-filled or operational). This cumbersome procedure is avoided when applying SPFEA. Furthermore, the GPFEA is based on the element resolution in the static analyses. In order to increase the element resolution at critical locations, the static

analysis must be repeated every time, again since new nodes cannot be defined when restarting an analysis. For an SPFEA solver any element resolution may be applied, with nodal coordinates of new nodes obtained by interpolation.

GPFEA solutions for long pipelines also require significant file storage utilization. An SPFEA solver may store only the data of interest, which may be several orders of magnitude smaller in capacity requirement than GPFEA. In addition, the SPFEA solver is faster than the GPFEA, especially considering that the static analysis only needs to be performed once. Since the purpose of the SPFEA solver is to perform parametric studies at a large scale, such issues related to computational efficiency and storage may be highly important.

Finally, the transparency of the physical modeling in the SPFEA solver is a big advantage in itself. When applying GPFEA software, there is always a risk that the user, not having access to the computer code, is unaware of certain aspects of the FE modeling.

# 7 CONCLUSIONS

- A specific purpose FEA (SPFEA) solver for modal analyses of offshore pipelines, based on input from a static bottom roughness analysis, has been developed. The SPFEA solver has been thoroughly verified based on comparisons to analytical results and to results obtained using commercially available general purpose FEA (GPFEA) software.
- Methodologies have been described for bottom roughness analyses and subsequent modal analyses of offshore pipelines resting on the seabed using GPFEA software.
- By comparing results of modal analyses performed with traditional Euler-Bernoulli beam elements and shear deformable PIPE31H elements, it has been shown that disregarding shear flexibility introduces negligible loss of accuracy in the calculation of eigenfrequencies and mode shapes for multi-span offshore pipelines.
- The SPFEA solver is a useful tool to study the effects of consistent versus lumped dynamic pipe-soil interaction effects. It has been demonstrated that the choice of consistent or lumped soil stiffness influences modal frequencies and mode shapes for representative realistic cases of pipes resting on rough seabed configurations.
- It has been demonstrated that the effect of added mass in axial direction is negligible even for pipes resting on terrain with a significant slope.


## ACKNOWLEDGEMENTS

The authors would like to extend their gratitude to Professor Jostein Hellesland at the University of Oslo for excellent discussions and revisions of the text.

## REFERENCES


Aamlid, O., Røneid S., 2008. "On-bottom roughness analysis with Abaqus", DNV report no. 2007-1148, DNV pipeline sections, Det Norske Veritas A/S, Høvik, Norway

Abaqus, v. 6.12, 2012. "Abaqus Analysis User's Manual", Dassault Systèmes Simulia Corp., Providence, RI, USA

Bergan, P.G., Syvertsen, T.G., 1989. "Knekning av søyler og rammer", Tapir, 2. opplag, ISBN 82 519-0254-1

Chopra, A.K., 2007. "Dynamics of structures: Theory and applications to earthquake engineering", Pearson Education, Inc., Pearson Prentice Hall, 3rd ed., ISBN 0-13-156174-X

Cook, R.D., Malkus, D.S, Plesha, M. E., Witt, R. J., 2002. "Concepts and applications of finite element analysis", Wiley, 4th ed., ISBN 0-471-35605-0

DNV-RP-F105, 2006. "Free Spanning Pipelines", Det Norske Veritas, Feb. 2006, Høvik, Norway

Fyrileiv, O., Mørk, K. , 2002. "Structural response of pipeline free spans based on beam theory", Proc. of 21st int. conf. on offshore mechanics and arctic engineering, OMAE 2002, June 23-28, Oslo, Norway

Fyrileiv, O., Mørk, K.J., Chezhian, M., 2005. "Experiences using DNV-RP-F105 in assessment of free spanning pipelines", Proc. of 24th int. conf. on offshore mechanics and arctic engineering, OMAE 2005, June 12-17, Halkidiki, Greece

Fyrileiv, O., Aamlid, O., Andreassen, E., 2010. "Pipeline free spans – influence of internal pressure", Proc. of 29th int. conf. on ocean, offshore and arctic engineering, OMAE 2010, Jun. 6-11, Shanghai, China

Hughes, T.J.R., 2000. "The Finite Element Method – Linear Static and Dynamic Finite Element Analysis", Dover Publications, Inc., Reprint, ISBN 0-486-41181-8

Kristiansen, N.Ø., Tørnes, K., Nystrøm, P.R., Damsleth, P., 1998. "Structural modelling of multi-span pipe configurations subjected to vortex induced vibrations", Proc. of 8th int. offshore and polar engineering conf., ISOPE 1998, May 24-29, Montreal, Canada

Matlab, v. 7.11, 2010. The MathWorks Inc.; Natick, MA, USA

Shames, I.H., Dym, C.L., 1991. "Energy and Finite Element Methods in Structural Mechanics: SI Units Edition", Taylor & Francis Group, 2nd ed., ISBN 0891169423

Sollund, H.A., Vedeld, K., 2012. "A semi-analytical model for free vibrations of free spanning offshore pipelines", Research Report in Mechanics, No. 12-2, Mechanics Division, Department of Mathematics, University of Oslo, Norway

Sollund, H.A., Vedeld, K., 2013. “A semi-analytical model for structural response calculations of subsea pipelines in interacting free spans”, Proc. of the Vth Int. Conf. on Computational Methods in Marine Engineering, MARINE 2013, B. Brinkmann and P. Wriggers (Eds.), Hamburg, Germany

Sumer, B.M., Fredsøe, J., 2006. “Hydrodynamics around cylindrical structures”, Adv. Series on Ocean Eng., Vol. 12, World Scientific, ISBN 9812700390

Vedeld, K., Sollund, H.A., Hellesland, J., 2013. “Free vibration of free spanning offshore pipelines”, Engineering Structures, 56, pp. 68-82

Vedeld, K., Sollund, H.A., Hellesland, J., Fyrileiv, O., 2014. “Effective axial forces in offshore lined and clad pipes”, Engineering Structures, 66, pp. 66-80

Zdravkovich, M., M., 1997. “Flow around circular cylinders, Vol. 1: Fundamentals”, Oxford science publications, Oxford university press, ISBN 978-0-19-856386-9